國立臺灣大學理學院物理學系

碩士論文

Department of Physics
College of Science
National Taiwan University
Master’s Thesis

催化劑輔助低溫化學氣相沉積合成二硒化錫之研究

Low-Temperature CVD Synthesis of Tin Diselenide with A Promoter

楊維弘

Wei-Hung Yang

指導教授：謝馬利歐 博士
謝雅萍 博士

Advisor: Mario Hofmann, Ph.D.
Ya-Ping,Hsieh, Ph.D.

中華民國 112 年 07 月

July 2023

doi:10.6342/NTU202301860

國立臺灣大學碩士學位論文
口試委員會審定書
MASTER'S THESIS ACCEPTANCE CERTIFICATE
NATIONAL TAIWAN UNIVERSITY

（論文中文題目）(Chinese title of Master's thesis)

催化劑輔助低溫化學氣相沉積合成二硒化錫之研究

（論文英文題目）(English title of Master's thesis)

Low-Temperature CVD Synthesis of Tin Diselenide with A Promoter

本論文係 楊維弘 (姓名) R10222068 （學號）在國立臺灣大學 物理 (系/所/學位學程) 完成之碩士學位論文，於民國 112 年 7 月 27 日承下列考試委員審查通過及口試及格，特此證明。

The undersigned, appointed by the Department / Institute of __________physics__________

on 27 (date) 7 (month) 2023 (year) have examined a Master's thesis entitled above presented by Wei-Hung, Yang (name) R10222068 (student ID) candidate and hereby certify that it is worthy of acceptance.

口試委員 Oral examination committee:

（指導教授 Advisor）

Chu Chi Ting

系主任/所長 Director:

doi:10.6342/NTU202301860

致謝

時光飛逝，短短兩年的碩士班的生涯已進入尾聲。回首當年進入國立台灣大學物理系攻讀碩士，並且進入中央研究院原子與分子研究所做研究的總總過程，我已在不知不覺中完成了我當科學研究員的夢想。

在此首先要感謝的是中研院原分所的謝雅萍老師，當時在我對未來研究方向還充滿不確定時，願意收我當研究生，讓我有嘗試新領域的可能。在我做研究時，我曾經在其中遭遇了許多困難跟挫折，也因此迷失了一段時間，但是老師仍然沒有因此而放棄我，也給予了許多的鼓勵，使我最終能夠完成這個研究。在研究指導方面，老師也給了我許多想法與知識，引導我撥雲見日，走出研究的霧裡。還要感謝 Mario Hofmann 老師，給予我許多實驗上的建議與推銷研究結果的能力，讓我體會到一個科學家做研究除了物理理論與實驗方法外，如何把做出來的研究結果介紹出去也是不可或缺的一環。

除了老師們諄諄教誨外，在研究的路途上也有一群優秀的實驗室前輩提供大量的協助，傳授我實驗的技巧。感謝定睿學長、浩廷學長、郁翔學長與逸凡學長教導我使用實驗儀器與做實驗時的一些技巧，我也時常與他們分享我做研究時的結果或困難，他們也不厭其煩地提供我建議與協助。感謝志龍大哥幫忙處理實驗室相關事宜，讓我們能有更多的時間能專注做實驗。

在同學中，也要感謝在原分所 218 實驗室的各位大哥的陪伴。感謝柏翰大哥時常熱心的協助實驗室中同學們的問題，我也常常受他關照。感謝姚博士郁祺跟我討論實驗的技巧與作報告時需要注意的細節。還有回想起與睿騰大哥、汪灝大哥、睦辰大哥、儒哲大哥還有建安大哥在 218 實驗室中共事的時光，一起拚實驗，一起玩模擬的日子，過的十分的充實，能在碩班生涯中與各位共事令我感到非常的榮幸。還要感謝耀偉大哥在我去物理系館生長材料的漫長等待時間，陪我聊天與分享研究成果，也時常在我的材料生長失敗時給我鼓勵。也感謝俊霖學長，立下了這個題目的基石，使我有個巨人的肩膀可以站立。

最後還要感謝我的父母，提供了很多資源，讓我無生活上的後顧之憂，使我順利完成碩士學位。

2023.07.15 楊維弘

doi:10.6342/NTU202301860

中文摘要

二維材料的領域日新月異，新興的材料與合成方法也不斷推陳出新。當中我們選擇熱電性質良好的二硒化錫作為研究對象，並且於先前研究中設計出以石墨烯催化低溫生長大面積、高品質的二硒化錫獲得極大成功。更低的生長溫度將降低生長時所需的能量消耗，以節約電能，並且有望使材料生長於低熔點的基板上。我們接續石墨烯催化的成功經驗，嘗試了以美耐皿海綿碳化形成的含氮多孔碳於低溫設置的化學氣相沉積合成法，沉積二硒化錫薄膜於熔融石英基板上。實驗結果顯示，由多孔碳催化的二硒化錫薄膜在 100°C 的溫度設置下有大面積及較好結晶。透過元素分析、拉曼光譜、吸收光譜及 X 射線光電子能譜確認了薄膜的成分為二硒化錫。而從原子力顯微鏡掃描中，我們發現催化生長出來的二硒化錫薄膜是多片單層二硒化錫結晶堆疊而成。

我們也檢驗了由此合成方式合成之二硒化錫薄膜的熱電性及在光偵測器的應用。在光偵測器應用中，由此方法合成之二硒化錫薄膜因其特殊的多層結構使其有著較低的載子遷移率，而有了很高的光響應率，這個高的光響應率優於多數的二硒化錫研究，並且是在低溫情況下的出最好的結果。

最後，由於生長出來的二硒化錫薄膜是多片單層二硒化錫結晶堆疊而成，可以預期在受到外應力導致形變時，層與層之間的距離將發生改變，進而影響電阻值，此一特性有望作為壓力應變計使用。由於壓力應變計需要使用可撓性的基板，我們將可以使用的低溫催化生長方法可以使二硒化錫薄膜生長在可撓玻璃上，並且在後續的實驗中成功證實了其電阻的可變性。由於催化生長的環境溫度較低，可以期望未來將二硒化錫薄膜生長在更加便宜且低熔點的可撓基板上，例如 ：PET 等塑膠基板。

關鍵詞 ： 二硒化錫、低溫催化生長、多孔碳、光偵測器、光反應、熱電材料、壓力應變計

doi:10.6342/NTU202301860

Low-Temperature CVD Synthesis of Tin Diselenide with A Promoter

Wei-Hung Yang

Advisor : Dr. Mario Hofmann

Advisor : Dr. Ya-Ping, Hsieh

Graduate Institute of Physics

National Taiwan University

Taipei, Taiwan

July 2023

doi:10.6342/NTU202301860

Abstract

The field of two-dimensional materials is evolution fast and new materials and synthesis methods are constantly being introduced. Among them, we chose tin diselenide, which has good thermoelectric properties, as the research object. In the previous research, we designed a large-area, high-quality tin diselenide catalyzed by graphene at low temperatures and got great success. Lower growth temperature will reduce the energy consumption required for growth to save electricity. It also gives us the possibility to make materials grow on a low-melting point substrate. Continuing the successful experience of graphene catalysis, we tried the chemical vapor deposition synthesis method of nitrogen-riched porous carbon formed by the carbonization of melamine sponge at low temperature, and deposited tin diselenide thin film on the fused quartz substrate. The experimental results show that the tin diselenide thin film catalyzed by porous carbon has a large area and better crystallization under the temperature setting of 100^{o}C. Through elemental analysis, Raman spectroscopy, absorption spectroscopy, and X-ray photoelectron spectroscopy, it was confirmed that the composition of the film was tin diselenide. From the scanning of the atomic force microscope, we found that the tin diselenide film grown by catalysis is stacked with multiple single-layer tin diselenide crystals.

We also examined the thermoelectric properties of the tin diselenide film synthesized by this new method and its application in photodetectors. In the application of photodetectors, the tin diselenide thin film synthesized by this method has a low carrier mobility due to its special multilayer structure and high photoresponsivity. This high photoresponse is better than most of the tin diselenide research, and it is the best result at low temperatures.

Finally, since the synthesized tin diselenide thin film is composed of stacking multiple single-layer tin diselenide crystals, when the external stress causes deformation, the distance between the layers will change and affect the resistance value. This feature may be used as a pressure strain gauge. Since the pressure strain gauge needs to use a flexible substrate, we will use the low-temperature catalytic growth method to grow the tin diselenide film on the flexible glass, and successfully confirm the variability of its resistance in subsequent experiments.

doi:10.6342/NTU202301860

Due to the low synthesis temperature of the material growth, we may make tin diselenide thin films grown on flexible substrates with cheaper and lower melting points in the future, such as plastic substrates such as PET.

Keywords: Tin Diselenide, Low Temperature-Catalytic Synthesis, Porous Carbon, Photodetector, Photoresponse, Thermoelectric Material, Strain Gauge.

doi:10.6342/NTU202301860

doi:10.6342/NTU202301860

Contents

doi:10.6342/NTU202301860

doi:10.6342/NTU202301860

doi:10.6342/NTU202301860

List of Figures

doi:10.6342/NTU202301860

doi:10.6342/NTU202301860

doi:10.6342/NTU202301860

doi:10.6342/NTU202301860

List of Tables

doi:10.6342/NTU202301860

doi:10.6342/NTU202301860

Chapter 1

Introduction

Two-dimensional materials find diverse applications, spanning electronics, gas storage/separation, catalysis, high-performance sensors, support membranes, inert coatings, and more.[16] In recent years, more and more two-dimensional materials have been synthesized since the single layer of graphene was exfoliated from graphite by Andre Geim's group in 2004.[17] As the fast development of material, to find a material with low cost, environment friendly, non-toxic, and well competitive in performing particular applications properties is demanded.[18]

There is a type of multi-layer semiconductor, in which layers are bounded by van der Waals force, called van der Waals semiconductors. Those layers can be separated by mechanical[19] or liquid-phase[20, 21] exfoliation so that we may

doi:10.6342/NTU202301860

obtain the single-layer semiconductor easily. However, the most common van der Waals semiconductors show limitations and compromise their technological development.[22] For instance, at room temperature (300k), MOS_2 and WS_2 have a poor electric mobility of a few tens of $cm^2V^{-1}s^{-1}$;[23] $PdSe_2$ [24] has a limited commercial potential due to the high price of Pd (on March of 2023, the average palladium price is 1530 USD per ounce); GaSe is easily to oxidation when it exposure under both LASER and air.[25] Thankfully, there is a kind of material satisfy the requirement of cheap, non-toxic, stable, and good thermoelectric properties, which is tin diselenide ($SnSe_2$). $SnSe_2$ is rich in earth reserves and environment friendly it has an obvious future advantage in nanoelectronics and optoelectronics because of its low cost.[9] Due to many advantages, $SnSe_2$ has many applications, such as photo detector,[26] lithium battery,[27] phase change memory[28] and solar cells[29]. To achieve and promote these applications, how to synthesize $SnSe_2$ thin films and even nanosheets more economically has become an important topic in materials science in recent years.

doi:10.6342/NTU202301860

1.1 Properties of Tin Diselenide

Tin diselenide ($SnSe_2$) is a transition metal dichalcogenides (TMDCs) material , an intrinsic n-type semiconductor with a wide range of band gaps (0.9 $\sim$ 2.04 eV).[10] It has a 2D CdI_2-type hexagonal structure ($a = b = 3.81$ $\mathring{A}$ and $c = 6.14$ $\mathring{A}$) and each $SnSe_2$ monolayer is hexagonal closely packed sandwich layers. Those layers are stacked with a periodicity of one layer of the tin atom and two layers of selenium atoms and the layers are bounded by van der Waals force.[30]

The Raman peaks of $SnSe_2$ are out-plane vibrational A_{1g} mode at 185 cm^{-1} and E_g mode. From the position of E_g peak, $SnSe_2$ can be divided into two types, 1T phase, and 2H phase, the crystal structure of the two phases is shown in figure 1.1. The E_g position at about 108 cm^{-1} is 2H-crystal; the E_g position at about 118 cm^{-1} is 1T-crystal. A report shows that the intensity of the A_{1g} peak decreases remarkably as the thickness decreases and the E_g peak position decreases slightly from 118.3 cm^{-1} to 112.6 cm^{-1} with the reduction in the layer number.[31] We may use the layer-dependent Raman spectra to judge the number of the $SnSe_2$ layers.

For the thermoelectric properties of single layer $SnSe_2$, at 300K, the theoretical intrinsic carrier mobility is 462.6 $cm^2V^{-1}s^{-1}$; it's better than MoS_2 and WS_2. The theoretical thermal conductivity of single layer $SnSe_2$ is also better than that of most van der Waals semiconductors, which is 3.82 $Wm^{-1}K^{-1}$.[32] The excellent thermoelectric properties of $SnSe_2$ makes it become an important role of thermoelectric material. Other properties of $SnSe_2$ was shown in table.1.1.

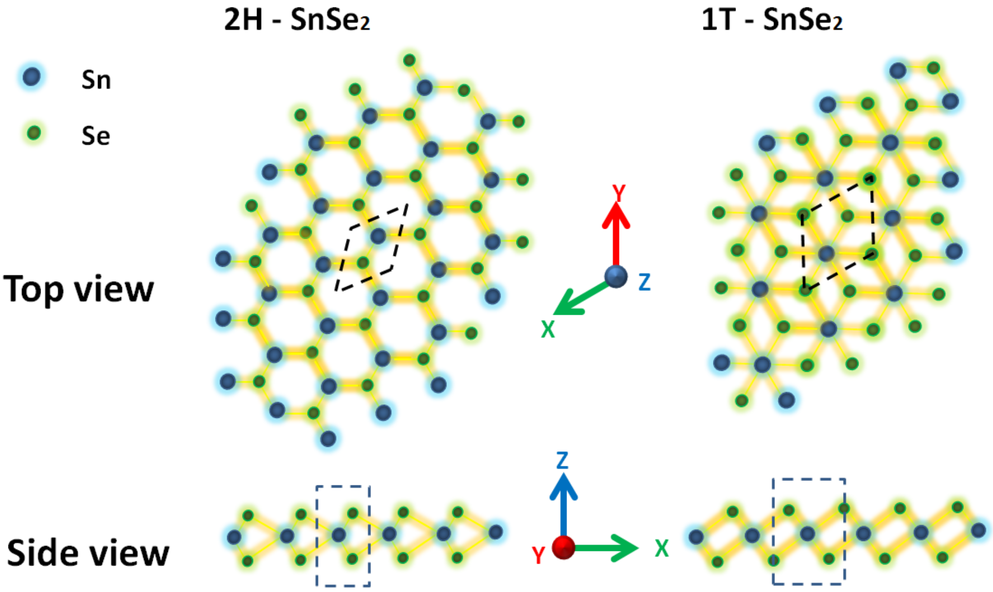

Figure 1.1: The top view and side view of the crystal structure of single layer 1T-phase and 2H phase $SnSe_2$. The blue spheres represent tin atoms, green spheres represent selenium atom and yellow lines are the chemical bonds.

Table 1.1: Properties of $SnSe_2$.[15, 10]

Semiconductor Type	n-type
Carrier Concentration (cm^{-3})	$10^{17} - 10^{19}$
Band Gap (eV)	$0.9 - 2.04$
Absorption Coefficient (cm^{-1})	10^{4}
Mobility (cm^{2}/Vs)	$0.6 - 85$

1.2 Research Motivation

1.2.1 Research Motivation

These days, we are facing the exhausting of energy resources problems. To synthesize material in a more efficient and lower energy cost way is an important issue. Reducing the growth temperature is a good way to save more power. Meanwhile, a low synthesis temperature also allows us to make $SnSe_2$ grow on a flexible substrate, which usually has a low melting point. It provides a new way to make a $SnSe_2$ based flexible device. In the traditional way, to make a flexible device, we have to synthesize a material on a high-temperature resistance substrate, then transfer the material to the flexible substrate.[33] It's a more complex method and the material may be damaged during the transfer process. If we can synthesize a material on a flexible substrate directly, making a flexible device would be easier.

doi:10.6342/NTU202301860

However, many reports show that it needs a high temperature (higher than 300^oC) to synthesize $SnSe_2$ by the CVD method.[9, 34, 35] Finding a new way to synthesis $SnSe_2$ at low temperature is a good research topic.

In earlier investigations, we found that graphene effectively promotes the growth of $SnSe_2$ with few layers over a large area at a low temperature (100^oC). The graphene-$SnSe_2$ hetero-junctions amplify electronic conductivity while reducing $SnSe_2$-related thermal conductivity. Additionally, the varying interaction at the $SnSe_2$/graphene interface leads to localized stress, introducing a unique strain sensing mechanism through 2D crack assistance. This mechanism's sensitivity surpasses that of other 2D materials.[33, 36] To extend this research, we tried to make $SnSe_2$ on other carbon materials, such as a 3D graphene foam, carbon nanotube, and porous carbon at low temperatures.[2] After the synthesis experiments, we found that there existed some shiny, black-silver films around those carbon materials on the soda lime glass substrate. Especially for porous carbon, the film almost covered the whole glass substrate. After we did many examinations, such as Raman spectra, SEM and EDX, and AFM, we identified that those films are many small $SnSe_2$ single-layer flakes stacked together. Normally, at such low temperature and without those carbon material, it was very hard to make high coverage

doi:10.6342/NTU202301860

SnSe$_2$ grow on glass substrate. Previous research also shows that synthesizing

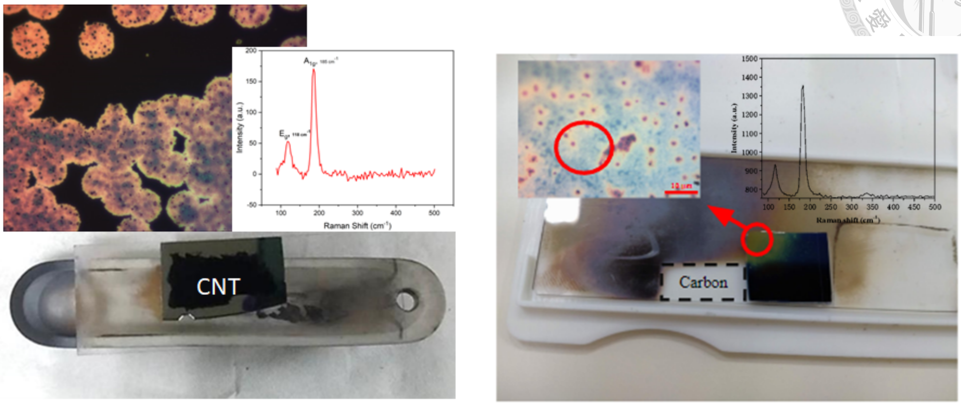

(a) (b)

Figure 1.2: (a) The outlook and optical microscope picture of SnSe$_2$ film grown on soda lime glass around the carbon nano-tube. The inset plot is the Raman spectra of the film and the spectra show the characteristic peaks of SnSe$_2$ (A$_{1g}$, 185 cm^{-1}; and E$_g$, 118 cm^{-1}). (b) Porous carbon promoted SnSe$_2$ film covers a large area of glass substrate. Some crystals have grown on SiO$_2$ substrates. The inset Raman spectra verify the film is SnSe$_2$.

SnSe$_2$ at low temperatures is very hard to make SnSe$_2$ grow on SiO$_2$/Si substrate due to the substrate temperature is not high enough.[37] This discovery gives us a hope to synthesis SnSe$_2$ at low temperature. We think that carbon is able to reduce the activation energy of the formation of SnSe$_2$ and the porous structure provides a large surface area to make the reaction more quickly. If we can synthesis SnSe$_2$ at a low temperature, we may try to make it grow on some flexible substrates that have a low melting temperature.

In this research, we are going to find the growth parameter of SnSe$_2$ for porous carbon promoter at low temperature. We use fused quartz as a substrate, it has amorphous structure. Then compare the difference of porous carbon promoted sample and no promoter sample.

1.2.2 Applications

We measure the photoresponse of the film grown on fused quartz, because polycrystalline $SnSe_2$ film is a good material for solar cell and photo detector. The result shows that $SnSe_2$ film on fused quartz promoted by porous carbon has a better photoresponsivity and response time than no promoter one, and other photo detector parameters are also greater than no promoter one.

We also tried to make $SnSe_2$ grow on a flexible substrate and checked the strain gauge factor of the $SnSe_2$ film, this can be applied to strain gauge.

1.3 Photodetector and Photoresponse

A photodetector is a device to detect light, it transfers received photons to a measurable electric signal. There are many types of photodetectors classified by mechanism of detection, including photoconductors, photodiodes, photoelectro-

doi:10.6342/NTU202301860

chemical devices, and phototransistors. Photodetectors are widely used in daily life, such as imaging, optical communication, and biomedical sensing.[38]

In practical applications, there is a significant demand for detectors with rapid response times. The response time primarily hinges on several factors: (1) the semiconductor's charge carrier mobility, (2) the depletion width for non-linear devices, and (3) the electrode distance for linear devices. [15] The response time of conventional Si and InGaAs photodiode is approximately 50 ps and a responsivity of about 500 mA/W at a maximum wavelength of 880 nm for Si photodiode and 1.2 A/W for InGaAs at 1550 nm. However, InGaAs have many drawbacks such as expansive manufacturing price, limited spectra range, non-transparency, etc.[39] Two-dimensional semiconductors are new materials to make photodetectors, they have high transparency due to the thickness of them are in atomic scale, good flexibility, strong light-matter interaction, and a low cost. For instance, graphene has a high charge carrier mobility of 2.5×10^5 $cm^2V^{-1}s^{-1}$[40], it makes an excellent response time of approximately 50 ps.[41] However, its high transparency makes low absorbance of IR and visible lights which is not a piece of good news for a highly efficient photodetector.

TMDCs are layered materials with properties that are band-gap dependent.

doi:10.6342/NTU202301860

They have a general formula of MX, M is some transition metals (such as W, Mo, Sn, In, Ga ...) and X is VIA group elements (usually S or Se). These materials can absorb a wide range of photon energy from 0.3 to 2.5 eV [42] and also have the advantages of 2D materials, now they have become an important role in photodetector.

1.3.1 Photoconductivity

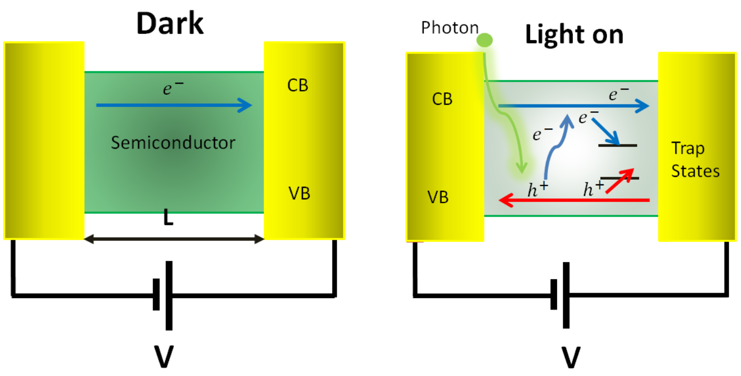

(a) (b)

Figure 1.3: (a) The schematic diagram of the photodetector set-up at dark environment and (b) at light-on environment. The the length L is the distance of two electrodes. Inside the semiconductor shows the schematic diagram of the band gap. The trap states in (b) is the key to modulate the resistance of the semiconductor. They capture free electron and holes to reach the effect of resistance modulation.

Photoconductivity is a phenomenon in which incident photons with energy exceeding the semiconductor's band gap are absorbed, creating energized free charge carriers that lower resistance. When a semiconductor is exposed to photons of higher energy than its band gap, electron-hole pairs form. These charge carriers are subsequently separated using an applied bias voltage. In the context of an Ohmic photoconductor utilizing a metal-semiconductor-metal configuration, the transit time is the period during which charges exist from generation until recombination or extraction. The measure of the response time, t_r, of the photodetector of the device shown in figure 1.3 is defined by:

$$t_r = \frac{L}{\mu E} = \frac{L^2}{\mu V} \tag{1.1}$$

where μ (in unit of $cm^2V^{-1}s^{-1}$) is the drift mobility, L is the gap of the two electrodes and E is the applied electric field. From eq.(1.1), we may conclude that a higher mobility, shorter electrodes distance and stronger electric field are helpful to reduce the response time. The photoconductive gain, G, defined as the ratio of the free photo-carrier lifetime to the transit time:

$$G = \frac{t_{car}}{t_r} = \frac{t_r \mu V}{L^2} \tag{1.2}$$

doi:10.6342/NTU202301860

where t_r is the response time (transition time) of free carriers and t_{car} is usually the life time of holes captured in trap state.[39] Those trap states act an important role to modulate the resistance of the semiconductor. They capture the holes and free electrons and localized them, and then form a local gate to modulate the resistance.[43]

1.3.2 Figures of Merit for Photodetectors

There are many types of figure of merits for photodetector:

- **Responsivity**

  The responsivity of a photodetector, $\mathscr{R}$, is an indication of the achievable electrical signal under certain illumination power. The unit of $\mathscr{R}$ is A/W. It's defined as the ratio of the output photocurrent or photovoltage to the input optical power on the active region of the device. The responsivity can be expressed as:

$$\mathscr{R} = \frac{I_{on} - I_{off}}{\mathscr{P}A} = \frac{I_{ph}}{\mathscr{P}A} \quad (A/W) \tag{1.3}$$

doi:10.6342/NTU202301860

where I_{on} and I_{off} are the currents of light on and off state, I_{ph} is the photocurrent and$\mathscr{P}$ is the power density (in unit of W/m^2) and A is the effective area.

- **Response and Recovery Time**

As we turn on the incident light, the output current signal is a raising drastically and then reaches a new balance level, the changing of photocurrent is ΔI. The response time, t_r is usually measured between $\pm 10\%$ of ΔI. As for the decay time, t_d, the measurement of t_d is just like the response time but we measure it as the light is turned off and the output current decay to the origin level.[15] For the application of a high-sensitivity photodetector, a small response time is favored.

- **External Quantum Efficiency**

The external quantum efficiency (EQE) is provide the efficiency of photon converts to photo current. The definition of EQE is the ratio of the number of electron-hole pairs, n_e, with contribution to the photocurrent to the total number of incident photons, n_{ph}. That is:

$$EQE = \frac{n_e}{n_{ph}} = \frac{\mathscr{R}hc}{e\lambda} \quad (\%) \tag{1.4}$$

where $\mathscr{R}$ is the responsivity, h is the Planck's constant, c is the speed of light, e is the elementary charge and λ is the wavelength of the incident light.

The EQE is the measure of the optical gain in the photodetector. A photodetector have higher EQE has a high optical absorption of the active layer, and a low carrier recombination and trapping rate before being collected.

- **Detectivity**

To compare the performance of photodetectors with different sizes and materials, we introduce the parameter called detectivity, D^*.

$$D^* = \frac{\mathscr{R}\sqrt{\mathbf{A}}}{\sqrt{2eI_{off}}} \quad (Jones) \tag{1.5}$$

where A is the effective area of a photodetector, which is the area of material between two electrodes. The unit of detectivity is Jones ($cm \cdot \sqrt{Hz}/W$) in honor of Robert Clark Jones who originally defined it.

An elevated detectivity signifies an enhanced performance of the photodetector.

1.3.3 Photodetectors Based on $SnSe_2$

Band gap, absorption coefficient, mobility, and device architectures play crucial roles in influencing photon absorption, responsivity, charge carrier transport, and separation performance. The fundamental characteristics of $SnSe_2$ are outlined in the table.1.1. This section provides some applications of $SnSe_2$ photodetectors.

Emma P. Mukhokosi's group developed $SnSe_2$ thin films on soda lime glass substrate and tuned the band gap to IR region (wavelength 1064 nm).[15] The responsivity is $2mA/W$ and the response/decay time are 7.76 s/ 2.5 s.

Peng Yu's group used bilayer $SnSe_2$ exfoliated from bulk single crystals onto SiO_2/Si substrates for photodetector and field effect transistor applications.[44] The experimental results show that it has a mobility of $4\ cm^2/Vs$ and on/off ratio of 1000 at $300k$. The response/decay time of the device are 2.1 ms/ 3.2 ms and a responsivity of $0.5\ A/W$. The lower response time and higher responsivity of $SnSe_2$ is due to the low mobility.

Manoj's group also developed $SnSe_2$ based photodetector with soda lime glass substrates. The device showed a responsivity of $0.8\ mA/W$ with response/decay times of 276 ms/332 ms and the slow response times may due to the trap states present in the system.[45]

1.4 Thermoelectric Material

Thermoelectric materials exhibit thermoelectric phenomena, encompassing the Seebeck effect, Peltier effect, and Thomson effect. These effects correspond to the following occurrences: the creation of an electric potential when a temperature difference is applied (Seebeck effect), the generation of heat flow through an electric current (Peltier effect), and reversible heating or cooling within a conductor under the presence of both an electric current and a temperature gradient (Thomson effect).

1.4.1 Seebeck Effect

The Seebeck effect is that: as we put two kinds of metals (or semiconductors) at different temperatures and contact each other, we may observe a current flow, like

doi:10.6342/NTU202301860

the condition in figure 1.4(a). The current flow is caused by charge carriers flow from the high charge carrier density side to the low charge carrier density side to eliminate the charge density difference. The charge carrier flow generates a voltage difference. For a semiconductor, the charge carriers can be electrons (n-type) or electron holes (p-type).

The carrier flow depends on the carrier density so that the Seebeck effect can also show in a single material. The density of free electrons in a metal is almost independent of temperature, while the charge concentration of the semiconductor, n_i, is a function of temperature:

$$n_i^2(T) = 4(\frac{m^* k_B}{2\pi\hbar})^3 T^3 e^{(-E_g/k_B T)} \tag{1.6}$$

where m^* (in unit of kg) is the effective mass of the charge carrier, $k_B = 1.38 \times 10^{-38}\ J/K$, T (in unit of K) is the temperature of the material and E_g (in unit of J) is the band gap energy; we may observe the voltage difference when we apply different temperatures on both sides of a semiconductor. Figure 1.4(b) shows the schematic diagram of Seebeck effect for a single material case. The voltage difference is called the Seebeck voltage, V_s. The formula of the Seebeck effect for

doi:10.6342/NTU202301860

a single material is given:

$$V_s = S\Delta T \tag{1.7}$$

where S (in unit of V/K) is the Seebeck coefficient, which represents the ability to convert heat to electricity, and ΔT (in unit of K) is the temperature difference between the two sides.

Since the Seebeck voltage is very small, we usually use the unit of $\mu V/K$ for convenience instead of the SI unit of V/K.

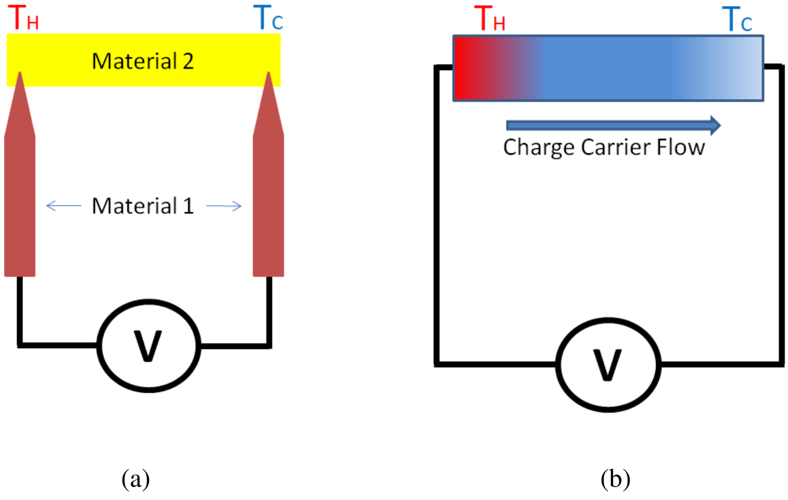

(a) (b)

Figure 1.4: (a) The schematic diagram of the Seebeck effect for two distinct materials. (b) The schematic diagram of the Seebeck effect for single material.

doi:10.6342/NTU202301860

1.4.2 Peltier Effect

As a charge current pass through two junctions a temperature difference will be generated, this is phenomena is called the Peltier effect. It's the reverse effect of the Seebeck effect.

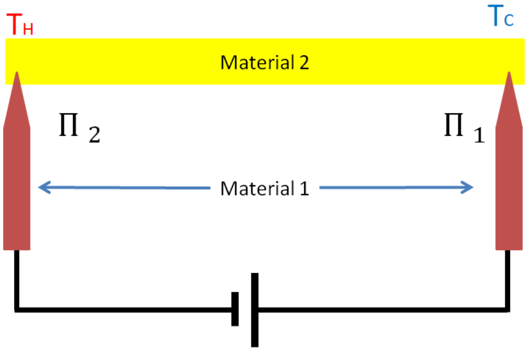

Figure 1.5: The schematic diagram of the Peltier effect of two distinct materials. In this case, $\Pi_1 > \Pi_2$. At one junction, there is the exothermic reaction; at the other, in contrast, is the endothermic reaction.

Figure 1.5 is the schematic diagram of the Peltier effect. The Peltier coefficient, Π (in unit of V), is expressed as:

$$\Pi = TS \tag{1.8}$$

where T and S are temperature and the Seebeck coefficient respectively. The

doi:10.6342/NTU202301860

Peltier coefficient is related to the heat transport per unit charge:

$$\frac{dQ}{dt} = I\Delta\Pi \tag{1.9}$$

where Q is the heat transfer (in J), I (in unit of A) is the current from passing through the two distinct materials and $\Delta\Pi$ is the Peltier coefficient difference between the two junctions.

1.4.3 Thomson Effect

The Seebeck coefficient varies in temperature for different materials. Therefore, the temperature gradient, $\nabla\mathbf{T}$, causes the gradient of the Seebeck coefficient, $\nabla\mathbf{S}$. As the gradient drives a current, we can observe a continuous Peltier effect. Figure 1.6 shows the Thomson effect and the thermoelectric reactions versus different temperature gradients. As the current flows from the low-temperature junction to the high-temperature junction, it's generating an exothermic reaction; as the current flow in the other direction, it's an endothermic reaction.

doi:10.6342/NTU202301860

The Thomson coefficient, $\mathscr{K}$, is given by:

$$\mathscr{K} = T\frac{dS}{dT} \tag{1.10}$$

where T is temperature and S is the Seebeck coefficient.

The formula of Thomson effect is:

$$\frac{dQ}{dt} = -\mathscr{K}\mathbf{J} \cdot \nabla\mathbf{T} \tag{1.11}$$

where Q is the heat transport, $\mathbf{J}$ (in unit of A/m^2) is the current density pass through the material and $\nabla\mathbf{T}$ (in unit of K/m) is the temperature gradient across the material. This equation describes how the temperature gradient and current flow direction affect the heat transfer in time.

1.4.4 Figure of Merit for Thermoelectric materials

The figure of Merit for Thermoelectric materials, as known as the ZT value, is a dimensionless coefficient to evaluate the efficiency of a thermoelectric material.

doi:10.6342/NTU202301860

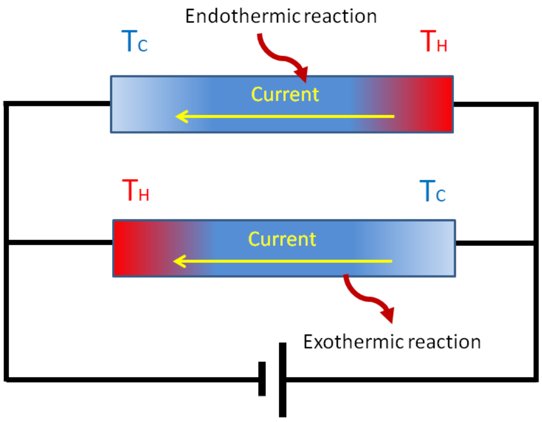

Figure 1.6: The schematic diagram of the Thomson effect. There are two direction of temperature gradients. As the current flows from low temperature junction to the high temperature junction, it's generating an exothermic reaction; as the current flow in the other direction, it's an endothermic reaction.

The definition of ZT value is given by:

$$ZT = \frac{\sigma S^2 T}{\kappa} \tag{1.12}$$

where σ (in unit of $\Omega^{-1}m^{-1}$) is the electrical conductivity of the material, S is the Seebeck coefficient, T is temperature of the material and κ (in unit of W/mK) is the thermal conductivity of the material. The term σS^2 in eq.(1.12) is defined as the power factor, PF. Higher PF can generate more energy from the temperature gradient.

For a great thermal material, the ZT value is higher. From eq.(1.12), to obtain a

doi:10.6342/NTU202301860

higher ZT, the electronic conductivity, and the Seebeck coefficient should be higher, and the thermal conductivity should be lower. A high electronic conductivity reduces the energy dissipation when a charge current flow through the material; meanwhile, a low thermal conductivity makes less heat dissipation.

1.5 Strain Gauges and Gauge Factor

1.5.1 Strain Gauges

Strain gauges are devices used to measure mechanical strain on an object. As we apply a deformation on an object, the strain gauge is also deformed and transduces mechanical strain into a changing electrical resistance. Nowadays, strain gauges have many applications in industries, especially in the oil and gas industry and automotive applications; the strain gauge market with a size of 4.5 billion USD.[46]

Since the 2D materials have excellent electrical, mechanical, and thermal properties, we may expand the application fields of 2D materials on strain engineering. For example, graphene film has been used to made a tunable gauge factors, low cost production and high sensitivity strain gauge.[46].

doi:10.6342/NTU202301860

1.5.2 Gauge Factor

The gauge factor (GF) is a coefficient that represents the relation between the electrical resistance change of the strain gauge and the mechanical strain. The mechanical strain is defined as:

$$\varepsilon = \frac{\Delta L}{L_0} \times 100\%. \tag{1.13}$$

Where ε (dimensionless) is the mechanical strain of the strain gauge, ΔL is the change in the length of the strain gauge and L_0 is the unstrained length of the strain gauge. The definition of GF is the ratio of the relative change of resistance to the mechanical strain:

$$GF = \frac{\Delta R/R_0 \times 100\%}{\varepsilon} \tag{1.14}$$

where ΔR (in Ω) is the change in electrical resistance of the strain gauge, R_0 (in Ω) is the unstrained electrical resistance of the strain gauge. GF is a dimensionless factor, we may obtain the factor from the slope of $\Delta R/R_0$-ε curve. The steeper slope corresponds to higher GF and better sensitivity of a strain gauge.

doi:10.6342/NTU202301860

Chapter 2

Synthesizing Experiments

In this chapter, we will demonstrate how to synthesize $SnSe_2$ by the chemical vapor deposition (CVD) method. The whole synthesis process mainly includes (a) the Production of carbon promoters. (b) Preparation of substrates and (c) Conduct CVD method to synthesize $SnSe_2$.

2.1 Production of Porous Carbon Promoter

To get a carbon promoter with a porous structure, we chose 99% melamine-formaldehyde resin sponge as a carbon source because it is cheap, easy to get, and has a porous structure. Then, we carbonized it at normal pressure in an argon gas environment. Figure 2.1 shows the OM image of porous carbon and Raman spectra of spot 1 and 2 in the OM image. There are three Raman peaks belong to carbon, a G band at 1583 cm^{-1}, a 2D band at 2600 cm^{-1} and a D band at 1350 cm^{-1}. A strong D band signal is due to the defect in the carbon structure.

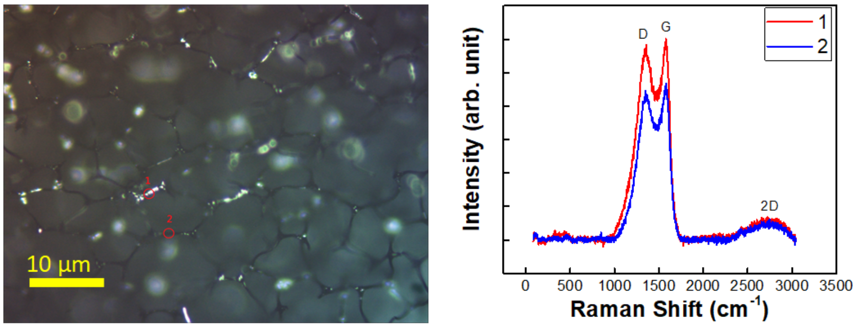

Figure 2.1: The OM image of the porous carbon and Raman spectra of the spots 1 and 2 in the OM image.

First, we cut the sponge into a suitable size, the promoter size we desire is $5mm \times 5mm \times 10mm$. Since the sponge gets shrunk to one-third of the original size after the carbonizing process, we usually cut sponges into $15mm \times 15mm \times 30mm$. Then sonicate them with alcohol for 10 minutes to remove any dirt attached to the surface. Next, use deionized water (DI water) to wash the sponges and put the cleaned sponges on a hotplate at 70^oC to drain. Then, put those sponges into the CVD furnace. Pumping out the air in the quartz tube and then inlet argon with a flow rate of 300 standard cubic centimeter per minute (sccm) until the pressure reaches 760 Torr. As the pressure reached the atmosphere, we start to heat the sponges with a heating rate of 1000^oC per 30 minutes and fixed the temperature at 1000^oC for 40 minutes, the argon gas remain at the same flow rate during the whole heating process. After the heating process, we cooled the furnace to room temperature naturally and took the porous carbon, a nitrogen-doped amorphous carbon promoter with porous structure, out.

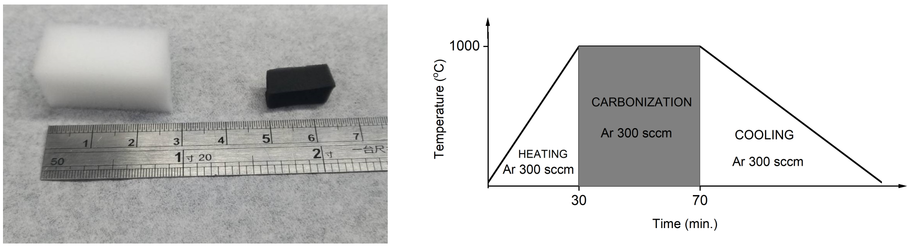

(a) (b)

Figure 2.2: (a) The melamine-formaldehyde resin sponge (left) and porous carbon (right). The size of dehydrated melamine-formaldehyde resin sponge (porous carbon) is shrink. (b) The temperature set up and gas flow for the carbonization of melamine-formaldehyde resin sponge.

2.2 Synethesis Tin Diselenide by CVD

2.2.1 Brief Introduction of Chemical Vapor Deposition

There are many ways to synthesize 2D-material. For example, we may use tape to mechanical exfoliate graphene from the bulk of graphite[47]; the liquid phase exfoliation technique is appropriate for cost-effective production of 2D materials with scalability, yet the dimensions and quality of solution-derived 2D materials raise considerations for specific applications.[21] Chemical vapor deposition (CVD) provides a method to synthesize large-scale, high-quality in a controllable and low-cost way. The main principle in CVD is precursor, which may be in the solid phase or gas phase, heated and become vapor; those vapor state precursors are reacting in the chamber or on the surface of the substrate and then deposited forming solid products.[48]

Several parameters come into play during the CVD growth of 2D materials, encompassing the choice of precursor, temperature, pressure, and substrate. The precursor functions as a reactant in the CVD process and involves thermal decomposition, chemical synthesis, and chemical transport reactions. In the context of solid-phase precursors, managing vapor concentration during CVD proves more

doi:10.6342/NTU202301860

challenging. Temperature constitutes another pivotal factor within the CVD process, influencing carrier gas flow rates, precursor reaction rates, and substrate deposition rates. Higher temperatures often lead to increased precursor concentrations due to enhanced evaporation over time. Furthermore, for nucleation at the vapor-solid interface, higher temperatures drive thermodynamic processes, while lower temperatures engage kinetic processes. Pressure constitutes another parameter tied to gas flow rates and precursor concentration. From the ideal gas equation,

$$PV = nRT \tag{2.1}$$

the concentration of precursor decreases with pressure decreasing. Moreover, at low pressure and fixed molecular flow rate, the gas flow speed and volume increase. Lower precursor concentration and higher precursor inlet rate are good for the control of the reaction. By adjusting these key parameters, we may control the product structure. For example, $SnSe_2$ nano-sheet has been reported that their shape and size change with temperature gradient and reaction pressure.[49]

The substrate is the place where deposits happen. Activate Substrate could be a catalyst that promotes product growth[50]; inert substrates are suitable for

doi:10.6342/NTU202301860

transition-metal dichalcogenide (TMDC) growth. For example, mica is used to synthesize a few layer $SnSe_2$ nanosheet in many reports[9, 34]. Due to the mica surface having no dangling bond, the migration barrier of the adsorbed atoms on its surface is much smaller than other substrates so that adsorbed atoms on the mica surface can migrate rapidly, thus making mica a suitable substrate for growing a few layers $SnSe_2$.[35]

2.2.2 Synthesis Tin Diselenide Experiment

To synthesize $SnSe_2$ by CVD procedure, some reports used tin selenide (SnSe) powder as the precursor.[51] However, we choose tin(II) iodide (SnI_2) powder and selenium (Se) powder as the precursor. Because SnI_2 has a lower melting point (320^oC) than SnSe (melting point = 861^oC) and some reports said that low melting point may be providing more uniform and stable growth conditions during CVD procedure.[9] Moreover, for tin, iodine was successfully applied for the growth of Cu_2ZnSnS_4 single crystals that are used in solar cell[52] and from the formula of reaction

$$SnI_2 + Se \rightarrow SnSe_2 + I_2 \tag{2.2}$$

doi:10.6342/NTU202301860

it was reported to be an optimal carrier agent [53]. The SnI_2 powder 100 mg and selenium powder 200 mg is placed on two sides of a tungsten boat respectively, the tungsten boat is placed on a aluminum boat. Then, put substrates with promoters and precursor into a quartz tube. Precursors are placed at the first temperature zone.

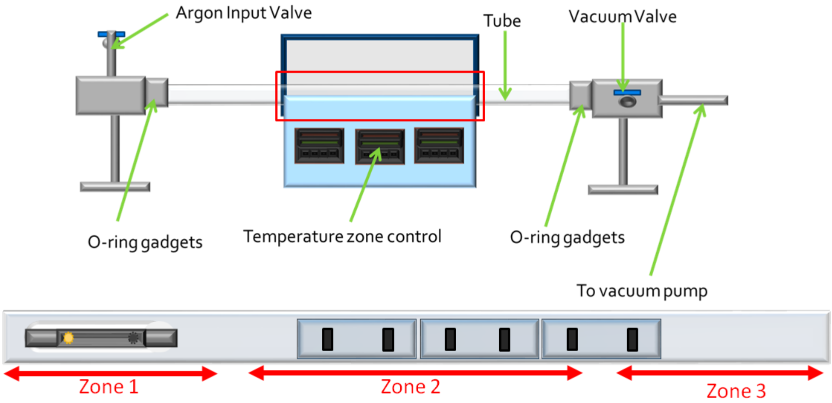

Figure 2.3: The schematic diagram of CVD equipments and original experimental set up.

To compare the temperature effect and how distance from the precursor affects $SnSe_2$ film growth, we put three fused quartz substrates at the second and third temperature zone. Each fused quartz substrate with a length of 76 mm and the promoters are placed at 12 cm, 16 cm, 20 cm, 24 cm, 28 cm, and 32 cm from the precursor on the fused quartz substrate. After placing precursors and substrates, we use argon gas to purge the gas in the quartz tube for 10 minutes. Then, vacuum the

doi:10.6342/NTU202301860

quartz tube until the pressure reach 0.03 Torr. There is no argon gas flow during the growth process. The schematic diagram of CVD equipments and experimental set up is shown in figure 2.3. Finally, we found that only the quartz slide at 11 cm to 18 cm has $SnSe_2$ film, so that we revised the experimental set-up in the following experiment. We only put one quartz slide and put porous carbon at 15 cm from the precursor.

The first temperature zone setting is heating to 120^oC in 3 minutes and sustaining at this temperature for 12 minutes to pre-heat the precursor; then, the temperature increase to 600^oC in 10 minutes and stops the heating process. The temperature setting for the second and the third temperature zones are identical, heating to 100^oC in 5 minutes and then sustaining at that temperature for 20 minutes. The total heating time is 25 minutes then the whole system is cooling to room temperature naturally. The schematic diagram of the revised experimental setup is shown in figure 2.4(a); the setting of temperature zones is shown in figure 2.4(b).

doi:10.6342/NTU202301860

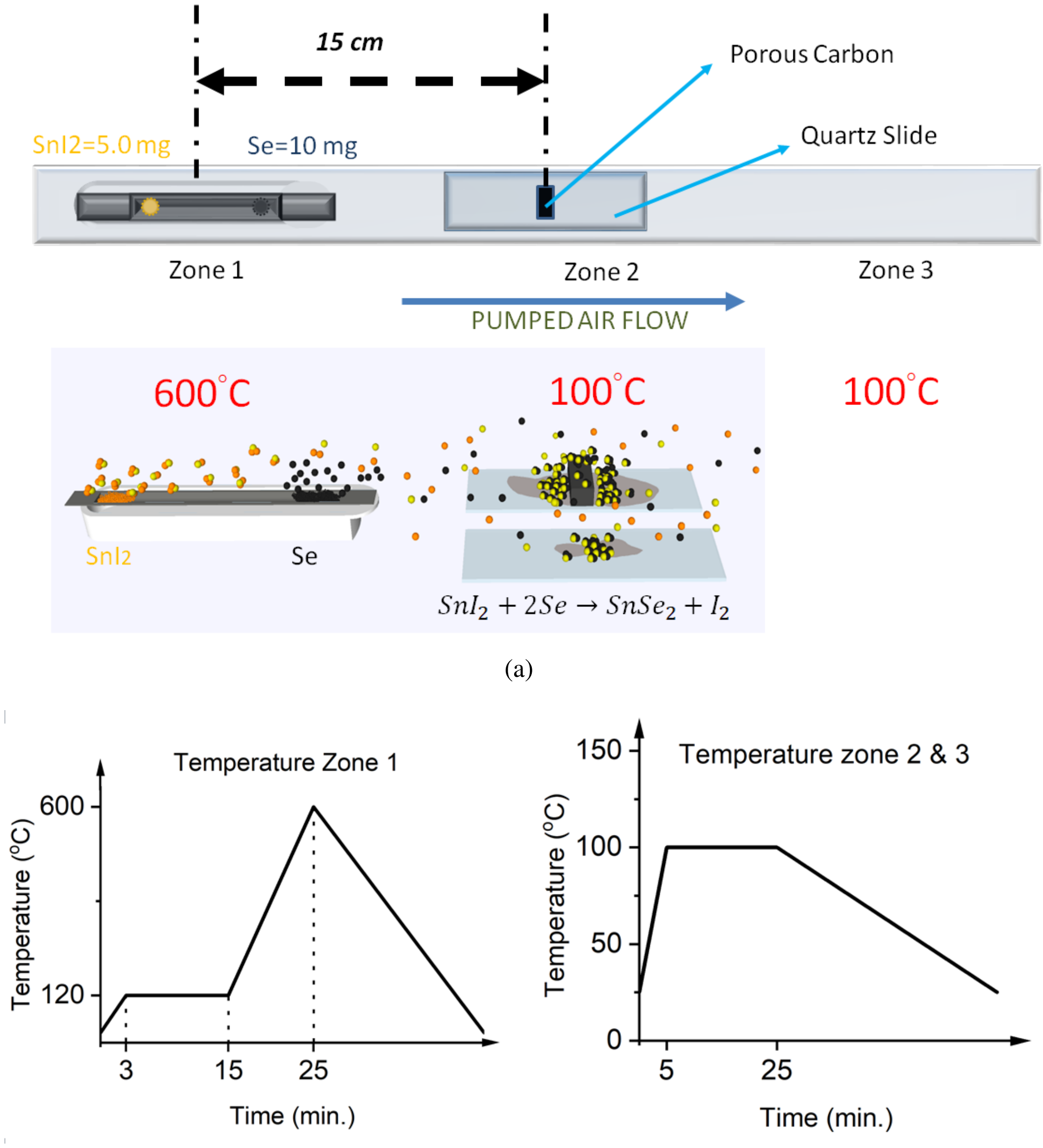

(a)

(b)

Figure 2.4: (a) The schematic diagram of revised CVD experimental set up and the reaction. (b) The temperature settings of temperature zone 1 (precursor is placed here) and temperature zone 2 and 3 (substrates are placed here).

Chapter 3

Apparatus And Analyses

After we synthesize $SnSe_2$ sample, we conduct a series of testing to check the characteristics and qualities of the sample. The first thing to do is take Raman spectroscopy to identify whether we synthesize $SnSe_2$ successfully; also, we can use scanning electron microscopy (SEM) or atomic force microscopy (AFM) to check the surface characteristics of the sample. Next, we examine the optical properties of the sample. We can obtain the band gap energy from the Tauc plot and the Urbach energy, which describes the energy states caused by amorphous and impurity. In this chapter, we demonstrate experimental apparatus in our lab and explain how they work; also, we show how we measure and analyze the measured data.

doi:10.6342/NTU202301860

3.1 Raman Spectroscopy

3.1.1 Scattering And Raman Effect

Scattering is an important issue in classical mechanics, electrodynamics, quantum mechanics and other fields. When a moving particle passes through a localized potential, its trajectory is affected by the potential and deviates from the original direction. We can say that the particle is scattered by the potential. In electrodynamics, the particle becomes an electromagnetic wave.

There are two kinds of scattering, elastic scattering, and inelastic scattering. In elastic scattering, the energy of the electromagnetic wave does not change in the whole scattering process, the scattered light has the same color and energy as the incident light but with a different propagating direction. One kind of elastic scattering is Rayleigh scattering. Rayleigh scattering is a scattering model established by Lord Rayleigh, it mainly treats the scattering process by small particles, such as gases and droplets. The total cross-section, which gives us the amount of an EM wave scattered, per molecular is given by:

$$\sigma \approx \frac{2k^4}{3\pi N^2}|n-1|^2 \tag{3.1}$$

doi:10.6342/NTU202301860

where k is the wave number (in unit of m^{-1}), N is the number of particle per volume and n is the index of refraction.[54]

We can make an estimation to the scattering cross-section of the scattering of air. Assume the environment is at the pressure 1.013×10^{-5} pa and temperature at 298k. From the ideal gas equation, $P = Nk_BT$, where N is the number of particles per volume and k_B is the Boltzmann constant, we have $N = 2.46 \times 10^{25}$ molecules per cubic meter. Suppose we use a LASER at wavelength $532nm$, which $k = 1.18 \times 10^{-7}\ m^{-1}$, as an incident light and the index of refraction of air is $n = 1.000293$, from eq.(3.1), we have a cross-section $\sigma = 5.8 \times 10^{-31}m^2$. In one cubic meter, about a fraction $\sigma N \approx 10^{-5}m^{-1}$ of the light will be scattered for every meter of travel.

n the course of a scattering process, not all photons undergo elastic scattering. Only a small fraction (approximately $1/1000$ of them) of the scattered photons deviates from the same frequency as the incident wave. Moreover, the intensity of Raman scattering stands at around 10^{-7} to 10^{-8} times that of the incident light. These particular photons are known as Raman scattered photons.[55] In 1928, Indian physicist Sir C.V. Raman ($1888 - 1970$) and his student, Sir K.S. Krishnan ($1898 - 1961$), made a significant discovery. They observed that when light

doi:10.6342/NTU202301860

interacts with a transparent material, the deflected light changes its wavelength and frequency. This phenomenon was coined the Raman effect or Raman scattering. As a result of this discovery, Raman was awarded the Nobel Prize in Physics in 1930. By analyzing the wavelength shift, valuable information about molecular vibration modes, molecular structure, symmetry, electronic environment, and more can be derived.

Suppose the incident light at frequency ν_o and the Raman scattered light at frequency ν_i, the change of energy is $\Delta E = h(\nu_i - \nu_o)$ corresponds to the energy absorbed (if $\Delta E < 0$) or gained (if $\Delta E > 0$) from the sample. The former is called Stokes radiation; the latter is called anti-Stokes radiation. The frequency change of light is called Raman shift. Figure 3.1 shows the mechanism of Raman scattering and the spectrum schematic diagram; in the spectrum, the left band is the Stokes line while the right band is the anti-Stokes line. The nature of Raman scattering is the interaction between photon and molecule; the energy level in Figure 3.1 can be the rotational or, typically, the vibrational energy level of a molecule. Raman shifts are usually reported in wave number, which unit is usually cm^{-1}. In order to convert between spectral wavelength and wave numbers of shift in the Raman

doi:10.6342/NTU202301860

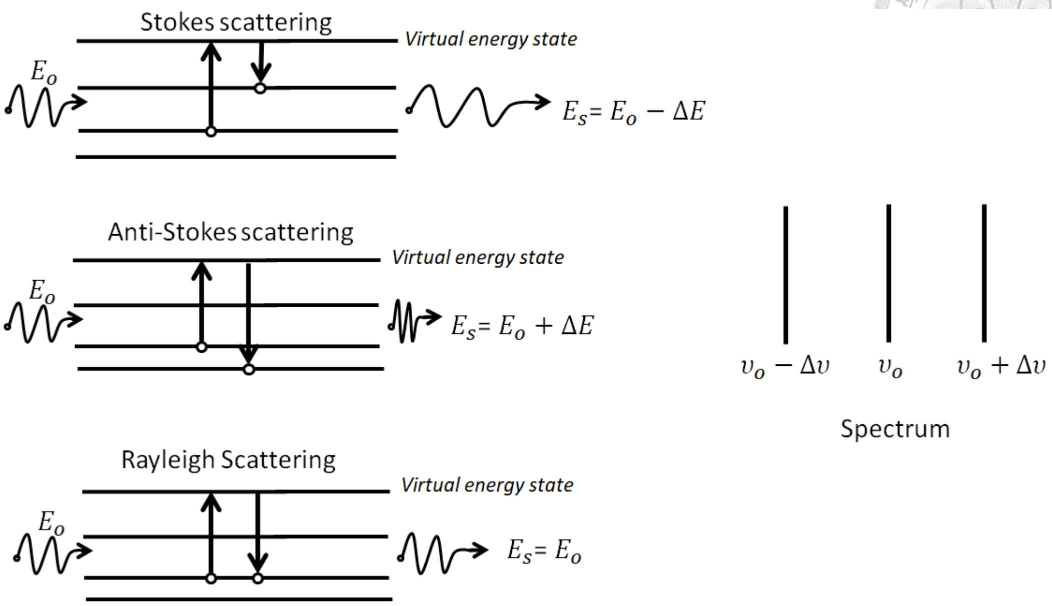

Figure 3.1: The mechanism of Raman scattering and the spectrum.

spectrum, the following formula can be used:

$$\Delta\tilde{\nu} = (\frac{1}{\lambda_o} - \frac{1}{\lambda_i}) \tag{3.2}$$

where $\Delta\tilde{\nu}$ is the Raman shift expressed in wave number, λ_o is the wavelength of the incident light and λ_i is the Raman spectra wavelength. Because we usually express the visible light wavelength in unit of nanometers (nm), eq.(3.2) can be scaled in the form:

$$\Delta\tilde{\nu}(cm^{-1}) = (\frac{1}{\lambda_o(nm)} - \frac{1}{\lambda_i(nm)}) \times \frac{10^7(nm)}{(cm)} \tag{3.3}$$

3.1.2 Raman Spectrometer

Before the invention of the laser, C.V. Raman and his student employed a mercury lamp and photographic plates to capture spectra. Owing to the limited strength of the light sources, the modest Raman cross-section, and the detectors' low sensitivity, they were required to dedicate extended periods (often hours or days) to obtain spectra. Given that the Raman effect holds weaker significance compared to Rayleigh scattering, the resulting photographic spectra remained largely dominated by a broad central line corresponding to the Rayleigh scattering of the excitation source.[56] Figure 3.2, clipped from C.V. Raman's article [1], shows the early Raman spectra of benzene; the broad line corresponds to the incident wavelength due to Rayleigh scattering.

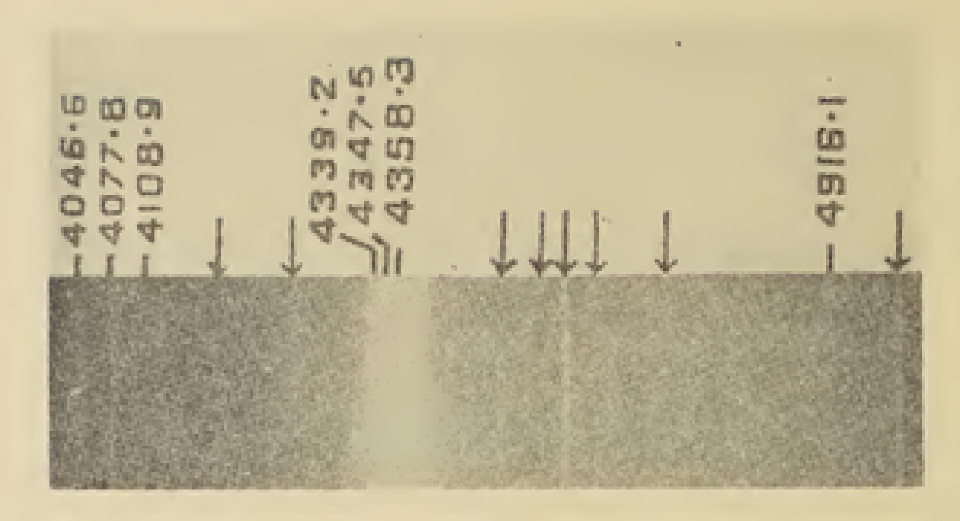

Figure 3.2: Early Raman spectra of benzene.[1]

Nowadays, LASER has been invented and used in Raman spectrometer as the light source. The light detector is no longer a photographic but a charge-coupled device (CCD). CCD is a device basically composed of a series of linked or coupled metal-oxide-semiconductor (MOS) capacitors; it receives photons and transfers them into electrons at the semiconductor-oxide interface then outputs electronic signals.

The Raman system in our laboratory (figure 3.3(a)) contains three main parts, the LASER system, optical microscopy (OM) system, and detector. In LASER system and OM system, a 532 nm LASER beam passes through an optical path to the object lens of the OM system rays on the sample. The scattered light received by the CCD detector and a program plots the Raman spectra. The spectra is only shows the Raman shift, Rayleigh scattering band is not shown in the spectra. The whole process only takes a few seconds. We can also use the Raman system to map a specific region of a sample. The mapping outcome tell us the distribution of certain compounds in the selected area.

doi:10.6342/NTU202301860

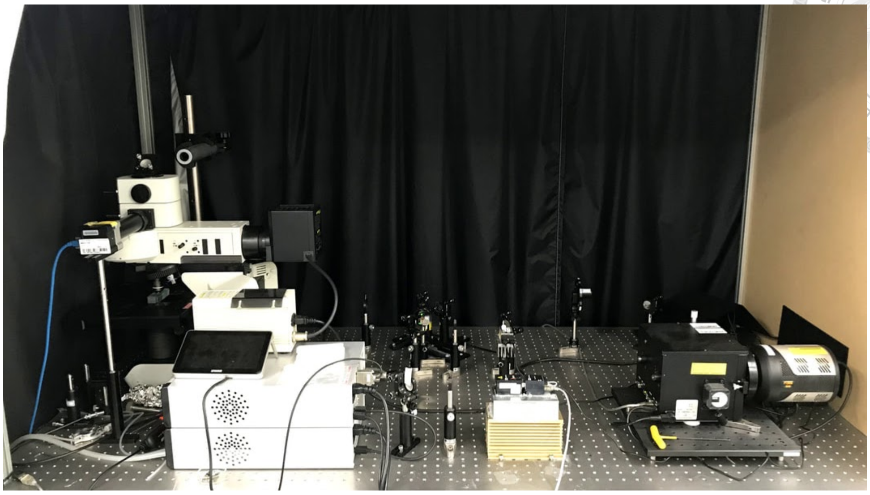

(a)

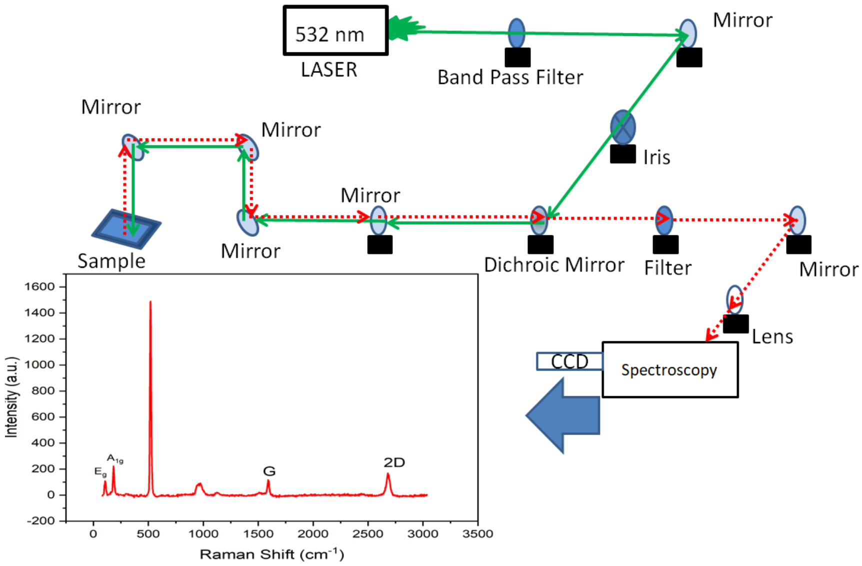

(b)

Figure 3.3: (a) The Raman System. (b) Light path schematic diagram. The green line is the light path of the 532 nm LASER, and the red dotted line is the light path of scattered light. The inset picture is the Raman spectra of $SnSe_2$ / graphene.

doi:10.6342/NTU202301860

3.2 Surface Characteristics Analysis

3.2.1 Atomic Force Microscope

The atomic force microscope (AFM) was invented by IBM scientists, G. Binnig, C. F. Quate, and Ch. Gerber, in 1985.[57] The purpose they invented the AFM was they want to make a non-conductor sample that could be scanned by a method like a scanning probe microscope (SPM). If we want to know the surface structure of a sample, the AFM helps us construct the topography. We may realize the surface characteristics of a sample from the topography, like the thickness or the shape of a 2D material flake.

The AFM system typically comprises a cantilever, a detector, and a sample stage. Positioned at the cantilever's end, there's a minuscule and delicate tip functioning as the probe, characterized by a curvature radius on the order of nanometers. This tip undergoes deflection as it approaches the sample's surface due to various forces at play, including mechanical contact force, van der Waals forces, capillary forces, chemical bonding, electrostatic forces, and magnetic forces. The selection of an appropriate probe type and imaging mode hinges on the specific context and the type of force to be measured.

doi:10.6342/NTU202301860

Speaking to the working principle of an AFM, we start from the probe-detector system. There is a low-power LASER ray shine on the tip. The tip is coated with a highly reflective layer so that some light reflects and shoots to the light detector. As the piezoelectric material-driven sample stage is scanned in the x-y direction, the tip deflects with the sample surface up and down, making the reflected light displacement. The feedbacked error signal proceeds by the controller and lets the z-axis of the sample stage move to make the reflected light remain in the same position. The z-direction moving would be processing and combined with the x-y direction information to form the topography.

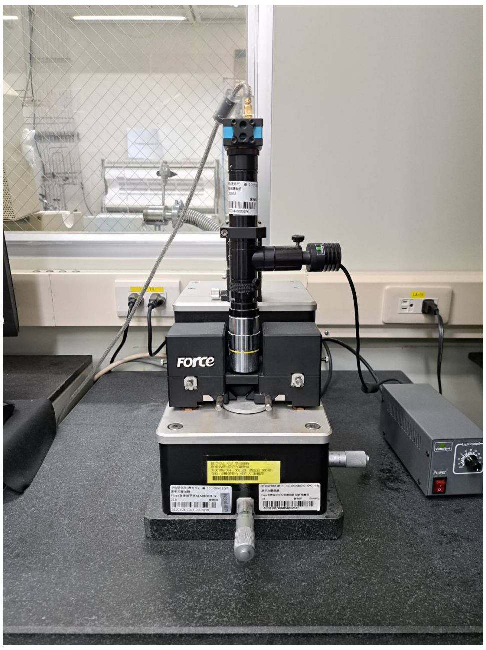

Figure 3.4: The AFM in our laboratory.

doi:10.6342/NTU202301860

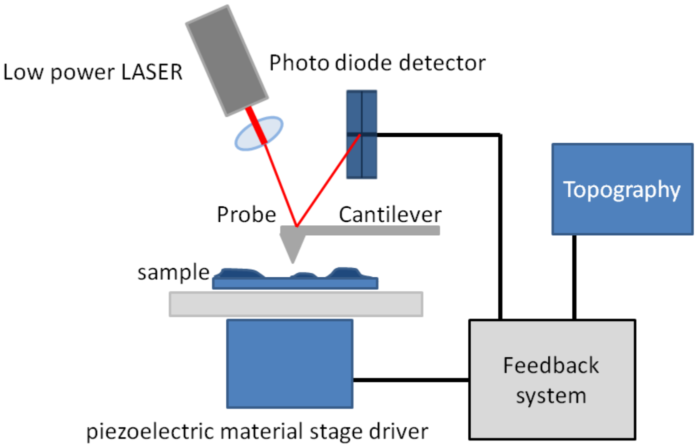

Figure 3.5: The configuration of an AFM.

3.2.2 Scanning Electron Microscope

A scanning electron microscope (SEM) is the other apparatus we usually use to let us know the surface properties of a sample. It's a type of electron microscope.

An SEM system contains a vacuum system, beam generator, beam manipulation, beam interaction, detector, signal processing, and display and record. The sample will be located on a stage in a vacuum circumstance to make the primary electron beam not be scattered by air molecules. The primary electron beam interacts with atoms at different depths on the sample and generates many types of electron signals. Those signal sources include secondary electrons, backscattered electrons, X-rays, visible light, and transmitted electrons. The secondary

doi:10.6342/NTU202301860

electrons are perhaps the most commonly used reaction event. They are generated by a primary electron beam dislodging a sample electron from the surface of the sample.[58] The generation of secondary electrons depends on the sample structure. The detector in SEM receives secondary electrons, and the signal processing system constructs the sample structure.

If we scanned a non-conductive sample, the electrons would be collected and accumulate charges on the sample. Those charges would increase until it reaches a critical point, and an electron discharge occurs and makes image artifacts.[58] To scan a non-conductive sample, we could make the surface grounded or coat a layer of metal (platinum, gold ...) on its surface.

An energy dispersive x-ray spectroscopy (EDS or EDX) usually be included in an SEM system. X-rays generated from the primary electron beam interact with the sample. The primary electrons excite the electrons in the inner shell in atoms on the sample surface and then form holes as electrons leave the inner electron shell. As outer shell electrons transit to the inner electron shell, excess energy becomes x-ray. EDX analyzes those x-ray emitted from different and tells us the concentration of each element in the sample.

doi:10.6342/NTU202301860

Figure 3.6: The SEM system in IAMS.

3.3 Optical Properties Examination

3.3.1 Absorption Spectroscopy

The band structure of a semiconductor can be probed by measuring its absorption spectrum since the electron transition from a lower energy state to a higher energy state absorbs a certain wavelength photon. There are many types of transitions in a semiconductor, such as band-to-band, excitations, sub-bands, between impurities and bands, etc. The absorption can be expressed as an coefficient, α (in unit of cm^{-1}).

The fundamental absorption process is the band-to-band process (or excitation

doi:10.6342/NTU202301860

transitions). The excitation transition obeys the selection rule; we may find the band gap of a semiconductor from the absorption edge. We have two main kinds of transition types for a semiconductor, direct transition, and indirect transition. The absorption coefficient can be express as a function of hc/λ:

$$\alpha(hc/\lambda) = K(hc/\lambda - E_g)^{\gamma}. \tag{3.4}$$

where $h = 6.626 \times 10^{-34}\ m^2\ kg\ s^{-1}$ is Planck constant, c is the speed of light, λ is the wavelength of light, K is a ratio constant and E_g is the band gap energy. For direct band gap, $\gamma = 1/2$; for indirect band gap, $\gamma = 3/2$.[59]

We use a self-made visible light spectrometer in our laboratory. The whole system is shown in figure 3.7. We put a sample on the stage of the microscope and use the built-in light in the microscope as the visible light source. A light receive lens connects with a fiber below the stage; the light signal is transmitted along the fiber and then received by a spectrometer (SEMSO-3000 Photoelectrochemical Synchronous Measurement System, BioLogic). Afterward, the spectrum is output to a computer.

The measured absorbance spectra is in unit of optical density (OD). The optical

doi:10.6342/NTU202301860

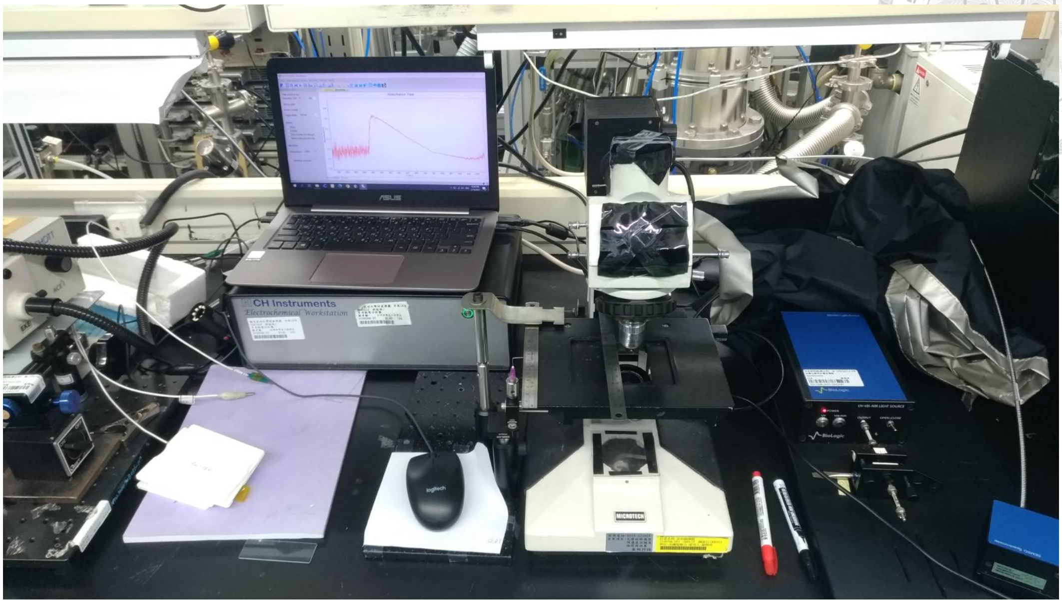

Figure 3.7: The self-made visible light spectrometer in our laboratory.

density, OD, is a logarithmic measurement of the percent transmission (T(%)) and it can be represented by the equation:

$$A(OD) = log(\frac{100}{T(\%)}) \tag{3.5}$$

That means for n OD, there are $10^{-n+2}\%$ of light to be transmitted through the sample. To transfer OD to absorption (ABS(%)), we have to get the transmission and then find the absorption by $ABS(\%) = 1 - T(\%)$. The transmission in percentage from eq.(3.5) is

$$T(\%) = 100 \times 10^{-A(OD)}\ (\%) \tag{3.6}$$

doi:10.6342/NTU202301860

From eq.(3.6), we can get the absorption (%) by:

$$ABS(\%) = 100(1 - 10^{-A(OD)})\ (\%) \tag{3.7}$$

3.3.2 Tauc Plot

To get the band gap from an absorption spectrum, we may use the Tauc method. The Tauc method was proposed by Jan Tauc in 1966, this method provides a way to estimate the band gap energy of amorphous semiconductors using optical absorption spectra.[60] This proposal was further developed by Davis and Mott.[61, 62]

The Tauc plot is a graph of $(\alpha h\nu)^{1/\gamma}$ v.s. photon energy [63], where α, γ and h is the same variable in eq.(3.4), $\nu = c/\lambda$ is the frequency of photon. By extrapolating a line of the straight interval and finding the intercept with the energy axis, where the intercept is the band gap energy. Figure 3.8 is a Tauc plot of SnSe2 film on an soda lime glass substrate. In figure 3.8, we use absorbance, A (in unit of optical density, OD), instead of the absorption coefficient; it does not affect the estimate of the band gap energy, because the relation between absorption

doi:10.6342/NTU202301860

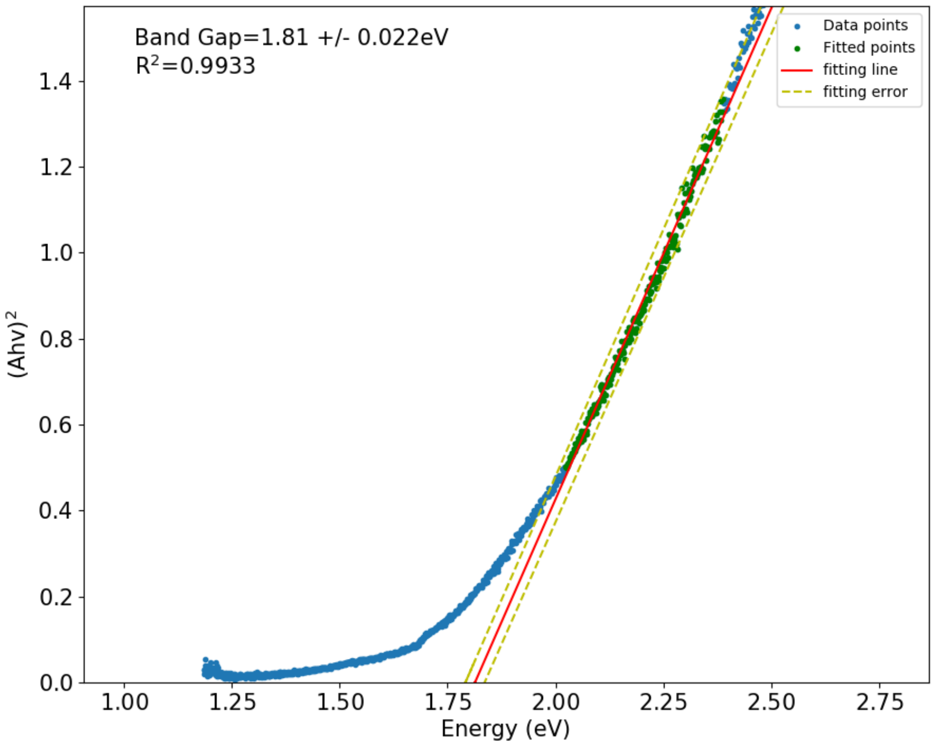

Figure 3.8: The Tauc plot of $SnSe_2$ film on a soda lime glass substrate. The yellow broken lines is the error bounds of the linear fitting, the red solid line is the fitted extrapolated line. The intercept of the red line with x-axis is the band gap energy. There is a tail in the lower energy of region of the absorption edge, which tail is the Urbach tail relate to energy states generated by amorphous or poor crystalline quality of a semiconductor.

coefficient and absorbance is:

$$\alpha(\lambda) = A(\lambda) \times 2.303/d, \tag{3.8}$$

where d is the thickness of the film, and we assume that the film thickness is uniform so that d can be seen as a constant. And the equation of the curve in the Tauc plot is :

$$(\alpha h\nu)^{1/\gamma} = \mathscr{A}(h\nu - E_g) \tag{3.9}$$

where $\mathscr{A}$ is a constant. From eq.(3.8), we have the relation that A is proportional to α, it only affects the scale of the curve but does not affect the intercept of extrapolated line with the energy axis. Substitute eq.(3.8) into Eq.(3.9), we have:

$$(Ah\nu)^{1/\gamma} = \mathscr{A}'(h\nu - E_g) \tag{3.10}$$

where $\mathscr{A}' = \mathscr{A}(d/2.303)^{1/\gamma}$ is the scaled constant of $\mathscr{A}$.

doi:10.6342/NTU202301860

3.3.3 Urbach Energy

Urbach energy is used to quantify energetic disorder in the band edges of a semiconductor. It has been proposed by Franz Urbach in 1953. He researched that there is a tail exponential increase in absorbance with energy along the absorption coefficient curve and near the optical band edge.[64] In further research, it has been discovered that the exponential tail appears in the poor crystalline quality, disordered, and amorphous materials because these materials have localized states which extend in the band gap.[65, 66]

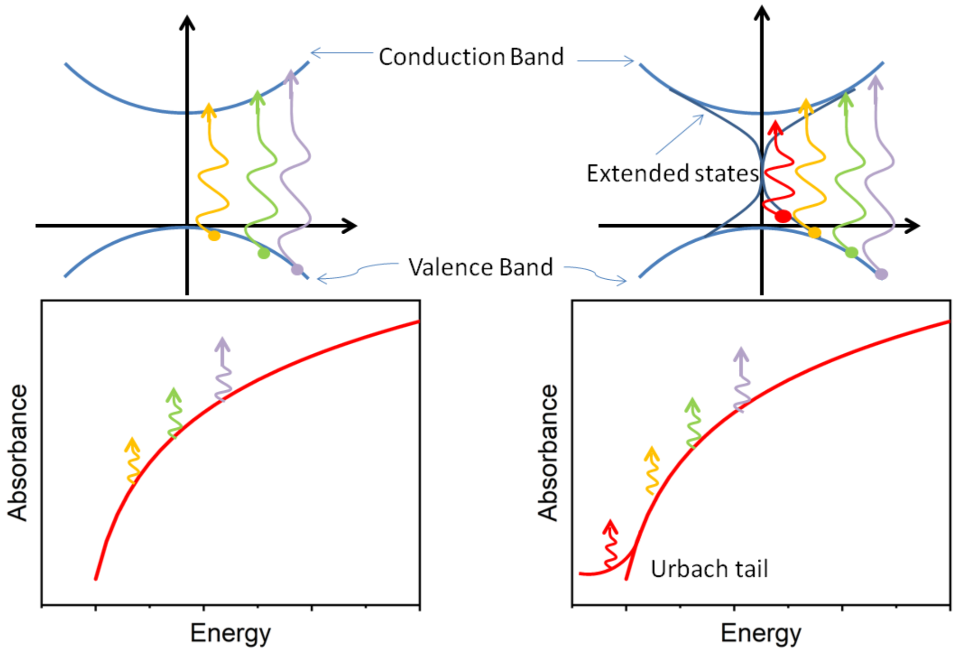

Figure 3.9: The schematic diagram of pure energy state and its absorbance edge (left); the schematic diagram of energy state with extended states and its absorbance edge (right). From their absorbance plot, we can see that the extended states absorb lower frequency light and form a tail in the low energy region.

doi:10.6342/NTU202301860

Figure 3.9 is the schematic diagram of the pure energy band and energy band with extended states; we also can see that the Urbach tail in the lower energy region of absorbance edge in figure 3.8.

The Urbach's rule can be used to relate to the absorption coefficient to the incident photon energy as following equation:

$$\alpha(\nu) = \alpha_0 e^{h\nu/E_U} \tag{3.11}$$

where α_0 is a constant, ν is the frequency of incident light and E_U is the Urbach energy. If we replaced α to A, eq.(3.11) can be written as:

$$A(\lambda) = A_0 e^{hc/E_U\lambda} \tag{3.12}$$

where A_0 is a constant and λ is the wavelength of the incident light.[67] We may get the Urbach energy from absorbance spectrum, rewrite eq.(3.12) as:

$$ln(A) = \frac{hc}{E_U\lambda} + ln(A_0) \tag{3.13}$$

and we have the relation of $ln(A)$ in function of $1/\lambda$. We can get Urbach energy in

doi:10.6342/NTU202301860

electron voltage (eV) from the slope of the linear region of the $ln(A)$-λ^{-1} curves using the equation:

$$E_U = \frac{1240}{slope\ in\ ln(A) - \lambda^{-1}\ plot}. \tag{3.14}$$

We use the least square method to fit the linear region of $ln(A)$-λ^{-1} curves and get the slope in eq.(3.14).

3.4 I-V Measurement

To measure the electrical properties of the synthesized sample, a current-voltage (I-V) measurement system is needed. The I-V measurement system in our laboratory can conduct the two-probe method, the MOSFET measurement, and the van der Pauw method.

3.4.1 Two-Probe Method

The two-probe method is used to measure the resistance of a sample. We also can find the conductivity of the sample from resistance. To conduct the two-point probe method, we have to make at least two electrodes on the sample. We usually use

doi:10.6342/NTU202301860

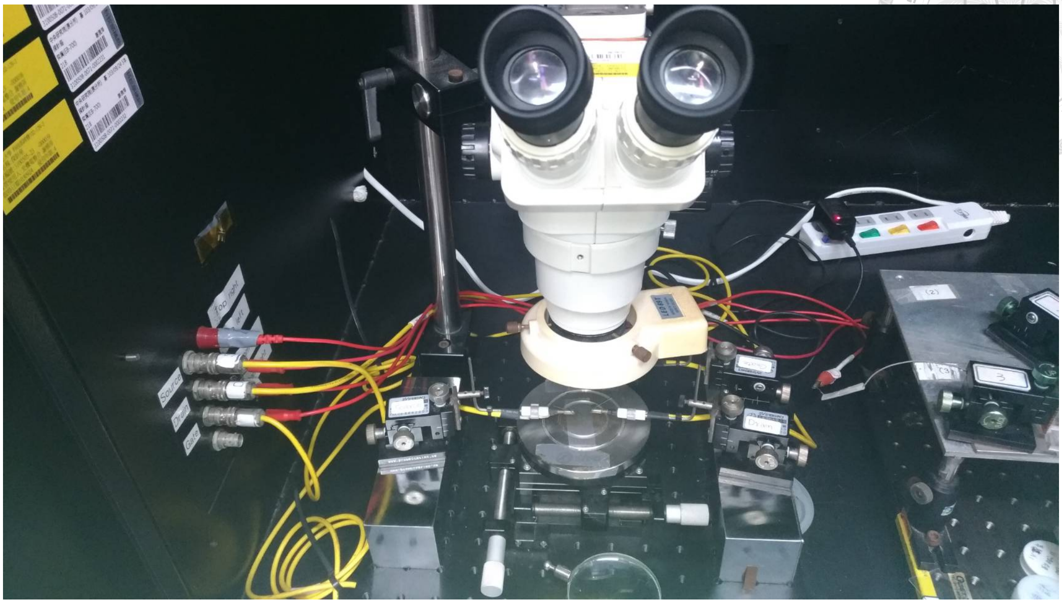

Figure 3.10: The two-probe method system in our laboratory. The optical microscope in the system makes us land the probe on the electrode more accuracy.

gold electrodes. We put the two probes on the two electrodes, then apply various voltages, such as from -1 to 1 V, and measure the current versus voltage to get an I-V curve. The ideal I-V curve for a Ohmic conductor is a straight line. The slope of the I-V curve, G, is the electrical conductance of the sample between the two electrodes. We may get the resistance by $R = \frac{1}{G}$. We may find the conductivity from the relation of resistance and resistivity:

$$R = \frac{\rho l}{wt} = \frac{l}{\sigma wt} \tag{3.15}$$

doi:10.6342/NTU202301860

where R (in unit of Ω) is the resistance of the sample, ρ (in unit of $\Omega \cdot cm$) is the resistivity, l is the gap between the two electrodes, w is the width of the electrodes, t is the thickness of the sample and $\sigma = \frac{1}{\rho}$ (in unit of S/m) is the conductivity of the sample.

3.4.2 The van der Pauw Method

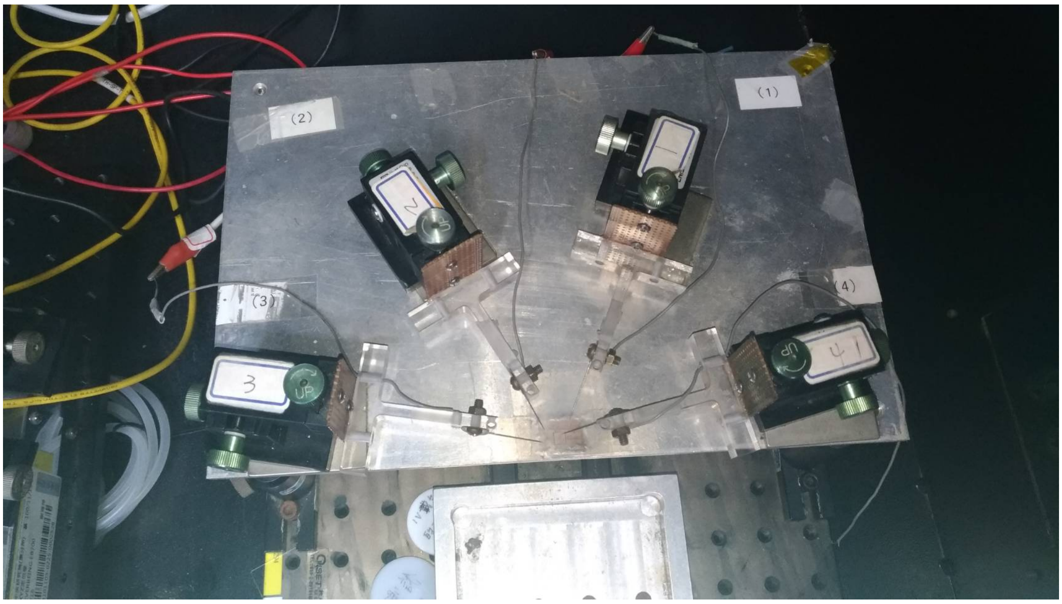

Figure 3.11: The van der Pauw method system in our laboratory.

We may find the sheet resistance of a film by conducting the van der Pauw (VDP) method (also called the four-point measurement). To conduct the VDP method, there are some requirements for the samples: (1) The film must be continuous, with no isolated hole. (2) Uniform thickness and thin film. (3) It needs four electrodes and the contact area of each electrode should be smaller than the film area by one order of magnitude. (4) The four electrodes must be located on the edge of the film. The four electrodes are numbered from 1 to 4 in counter-clockwise order, beginning at the top-right. To make a measurement, a current is applied to flow along one edge of the sample (for example, from electrode 1 to electrode 2, I_{12}) and measuring the voltage across the opposite edge (V_{34}). Resistance can be found in Ohm's law:

$$R_{12-34} = \frac{V_{34}}{I_{12}} \tag{3.16}$$

R_{1234} is the resistance along the horizontal edge, we may use the same way to find the resistance along the vertical edge, R_{2341}. To eliminate the effect of any offset voltages, such as thermoelectric potentials due to the Seebeck effect, and get a more accurate measurement, we repeated the resistance measurements after switching the polarities of both the current source and the voltage meter. Then, the resistances of the horizontal edge and the vertical edge are:

$$R_h = \frac{R_{12-34} + R_{34-12} + R_{21-43} + R_{43-21}}{4} \tag{3.17}$$

$$R_v = \frac{R_{23-41} + R_{41-23} + R_{32-14} + R_{14-32}}{4} \tag{3.18}$$

Finally, the sheet resistance, R_s, is related to these resistances by the van der Pauw formula:

$$e^{-\pi R_v/R_s} + e^{-\pi R_h/R_s} = 1 \tag{3.19}$$

for the special case: $R_v = R_h = R$, $R_s = \pi R/ln2$. In general case, we may calculate R_s by the Newton-Raphson method, an iterative method:

$$R_{s,n+1} = R_{s,n} + R_{s,n}^2 \frac{1 - e^{-\pi R_v/R_{s,n}} - e^{-\pi R_h/R_{s,n}}}{\pi(R_v e^{-\pi R_v/R_{s,n}} + R_h e^{-\pi R_h/R_{s,n}})} \tag{3.20}$$

The VDP method also can measure the Hall effect, carrier concentration and mobility. As the charge carriers flow through a magnetic field normal to the flow direction, the Lorentz force, F_L, experienced by the carriers is:

$$F_L = \frac{IB}{nA} \tag{3.21}$$

where I is the current, B is the magnitude of the magnetic field, n is the carrier concentration and A is the cross section of the sample. The charge accumulation will create an electric field across the material due to the uneven distribution of

doi:10.6342/NTU202301860

charge. The potential generated by the electric field is called the Hall voltage, V_H.

$$V_H = \frac{IB}{nqt} = \frac{IB}{qn_s} \tag{3.22}$$

where $q = 1.6 \times 10^{-19}\ C$ is the elementary charge, t is the thickness of the material and $n_s = nt$ is the sheet density, the density of electrons multiplied by the thickness of the material.

To measure the Hall voltage, we need to conduct two sets of measurements: one with a magnetic field in the positive z-direction, and one with it in the negative z-direction. The voltages recorded with a positive field will have a subscript P (for instance, $V_{12P} = V_{2P} - V_{1P}$) and those recorded with a negative field will have a subscript N. The applied current and the magnitude of the magnetic field must be kept the same for both measurements. We first apply I_{13p} and measure V_{24P} and then apply I_{31P} and measure V_{42P}. Repeat the steps to find V_{13P} and V_{31P}. Next, reverse the magnetic field and measure $V_{13N},\ V_{31N},\ V_{24N},\ V_{42N}$. We can take advantage of the reciprocity theorem to provide a check on the accuracy of these measurements, that is, $V_{13N,P} = V_{31N,P}$ and $V_{24N,P} = V_{42N,P}$. To calculate the Hall voltage, we start from the difference of the voltages for positives and negative

doi:10.6342/NTU202301860

magnetic fields:

$$V_{jk} = V_{jkP} - V_{jkN}, j = 1, 2;\ k = 3, 4. \tag{3.23}$$

and the Hall voltage is:

$$V_H = \frac{V_{13} + V_{31} + V_{24} + V_{42}}{8}. \tag{3.24}$$

If $V_H > 0$, the material is p-type; if $V_H < 0$, the material is n-type. The sheet density can be calculated:

$$n_s = \frac{IB}{q|V_H|}. \tag{3.25}$$

The unit of B is Wb/cm^2 if n_s is in cm^{-2}.

The resistivity of a semiconductor is given by:

$$\rho = \frac{1}{q(n\mu_n + p\mu_p)} \tag{3.26}$$

where n and p are the concentration of electrons and holes in the material respectively; μ_n and μ_p are the mobility of the electrons and holes respectively. In general, the two concentrations have many orders-of-magnitude difference so that eq.(3.26)

doi:10.6342/NTU202301860

is approximately equals to:

$$\rho = \frac{1}{q(n_m \mu_m)} \tag{3.27}$$

where n_m and μ_m are the doping level and mobility of the majority carrier respectively. For a semiconductor film, the sheet resistance $\rho = R_s/t$, where t is the thickness of the film; and $n_s = nt$. Eq.(3.27) can be expressed as:

$$R_s = \frac{1}{q n_s \mu_m} \tag{3.28}$$

and we can calculate μ_m by rearrange eq.(3.28):

$$\mu_m = \frac{1}{q R_S n_s}. \tag{3.29}$$

doi:10.6342/NTU202301860

3.5 Other Apparatus

3.5.1 Photo Lithography System

Figure 3.12: The photo lithography system in our laboratory.

Figure 3.12 is the photo lithography system in our laboratory. Photo lithography is an important technique to our research, we use it to make electrodes on our samples so that we are able to measure the thermoelectric properties of the sample.

The following steps are the photolithography process: (1) Spin coating photoresist on the sample. Photo resistance can be divided into two kinds, the positive photoresist, and the negative photoresist. Since the photoresist is sensitive to white light, we have to do photolithography in a yellow light environment. The positive photoresist will dissolve in the developer after exposure; while the negative

doi:10.6342/NTU202301860

photoresist is in contrast. We usually use the positive photoresist. (2) Design the pattern of the electrodes and then use the projector to expose the pattern on the sample. (3) Washing the sample by the developer and DI water. Then check the sample, we should see that the electrode pattern part is not covered for the positive photoresist case.

3.5.2 Thermal evaporator

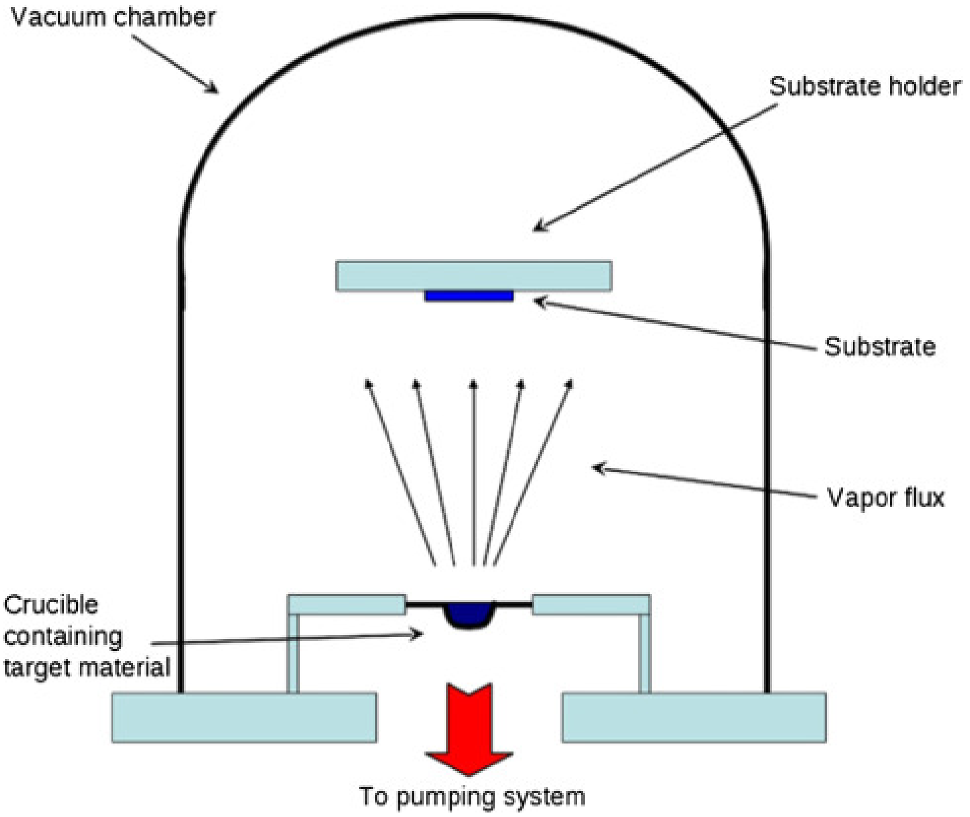

Figure 3.13: The schematic diagram of the thermal evaporator. [68]

After we made the pattern of electrodes, we need to coat some metal on the

doi:10.6342/NTU202301860

sample to fill those patterns. We are using a thermal evaporator to reach the target.

We put a metal nugget, for instance, gold, on a crucible and there is a sample holder above the crucible, the sample will be put on the sample holder face to the crucible. Then we are pumping the system to a low pressure (10^{-6} Torr) so that there are fewer other molecules. The crucible is connected to an electronic current source, the current will heat the crucible to melt the metal and make the metal evaporates. Those evaporated metal atoms move to the sample. There is a coating thickness gauge that shows the film thickness and the coating rate. To make an electrode, the film thickness should be 40 nm - 100 nm. Figure 3.13 shows the schematic diagram of the thermal evaporator.

After the thickness is reaching our requirement, we stop the heating process and take the sample out. Then remove the photoresist by taking an acetone bath. The rest part is the electrodes on the sample.

doi:10.6342/NTU202301860

Figure 3.14: The thermal evaporator system in our laboratory.

doi:10.6342/NTU202301860

Chapter 4

Result and Discussion

In this work, we provide a new way to synthesis $SnSe_2$ at low temperature by CVD method. In this chapter, we will discuss separately in two main sections: (1) the synthesized material's characterization and (2) the applications in photodetector and strain gauge.

4.1 Characterizations of Material

In this section, we discuss the differences between $SnSe_2$ film with and without porous carbon promoter. Those differences include absorbance intensity, Raman intensity, Urbach energy, EDX analysis, and the AFM image. The absorbance

doi:10.6342/NTU202301860

spectra mapping shows the distribution of thickness, the thicker thickness has higher absorbance intensity for the same material with the same absorption coefficient. The Urbach energy mapping can be extracted from the absorbance spectra mapping so that we may find the best crystalline region. Raman mapping reveals the distribution of $SnSe_2$ growth situation. SEM and EDX give us the sample surface structure and stoichiometric composition. The AFM image provides the morphology of the $SnSe_2$ film.

4.1.1 Absorption Spectra Mapping

First is the absorption spectra mapping.

After the synthesis experiment, we found that only the substrate on the 10 cm to 18 cm has $SnSe_2$ film. Based on the result, in further experiments, we put the porous carbon at 15 cm from the precursor. The synthesized sample's outward appearance is shown in figure 4.1. In figure 4.1 We may see that near the porous carbon, the coverage range is larger than the no promoter-assisted one and the film color is also darker than the no promoter-assisted one. A darker color can be attributed to thicker film thickness. Meanwhile, from the absorption mapping (figure 4.2, bottom) we may see that the absorption is gradually increasing on the

doi:10.6342/NTU202301860

interval of 130 mm to 145 mm from the precursor; while the absorption of the no promoter sample is decreasing to a small value in the same interval.

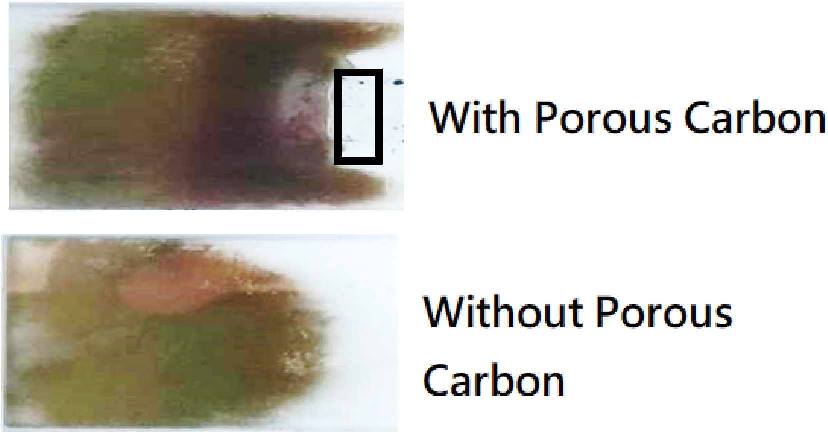

Figure 4.1: The outward appearance of the two samples with/without a promoter. The black rectangular is where the porous carbon is located. We may see that near the porous carbon, the coverage range is larger than the no promoter-assisted one and the film color is also darker than the no promoter-assisted one.

The absorption lines for both samples on the interval of 120 mm to 130 mm have the same trends. It shows that the promoter has less effect in the region. The less effect can be attributed to two possible: (1) the distance is too far from the promoter and here is the upstream region so the intermediates or products are hard to arrive here. (2) The temperature in this region is around $310^{o}C$ which is higher than that in 130 mm to 140 mm intervals (only around $250^{o}C$) so the temperature effect is higher than the promoter effect.

Next is the Urbach energy mapping (figure 4.2, top) also shows a considerable

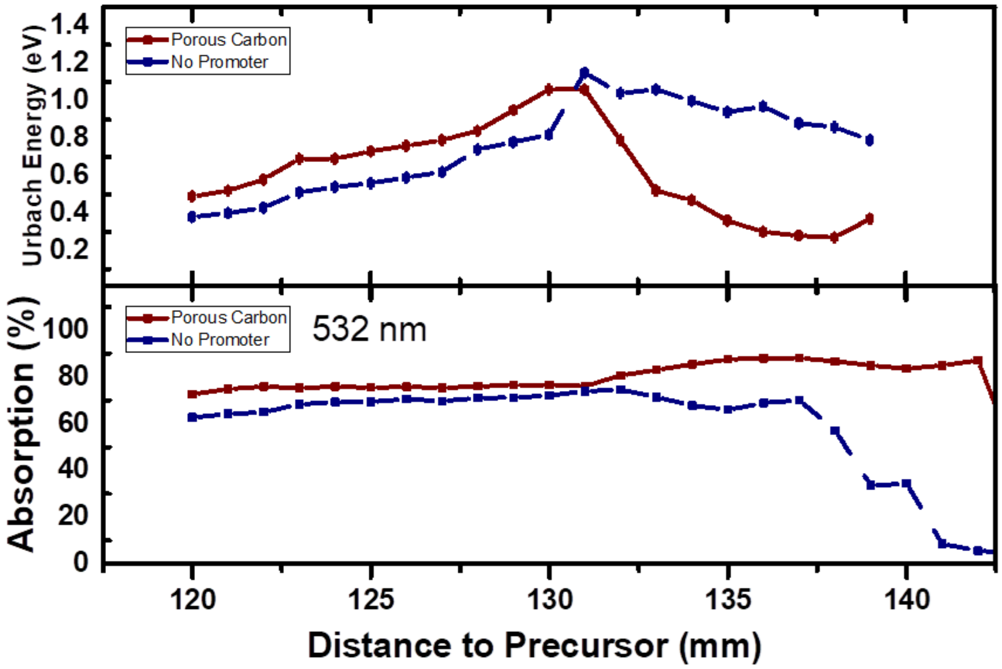

Figure 4.2: The bottom plot is the absorption spectra mapping of the sample with (wine solid line and scatter)/without (navy dashed line and scatter) porous carbon at 532 nm wavelength. The top plot is the extracted Urbach energy.

doi:10.6342/NTU202301860

difference in the 130 mm to 145 mm low-temperature interval. The Urbach energy is related to the energy states generated by defects in the crystal. A lower Urbach energy material has less defect. The porous carbon-assisted $SnSe_2$ film has much smaller Urbach energy than that of no promoter one. The minimum value of the Urbach energy for the porous carbon-assisted film has been found at 137 mm from the precursor which is 0.27 eV, however, in the same position, the Urbach energy for the no promoter-assisted film has a value of 0.88 eV. The Urbach energy fitting is shown in figure 4.3(b). It shows that the porous carbon promoter is increasing the crystalline quality of the $SnSe_2$ film.

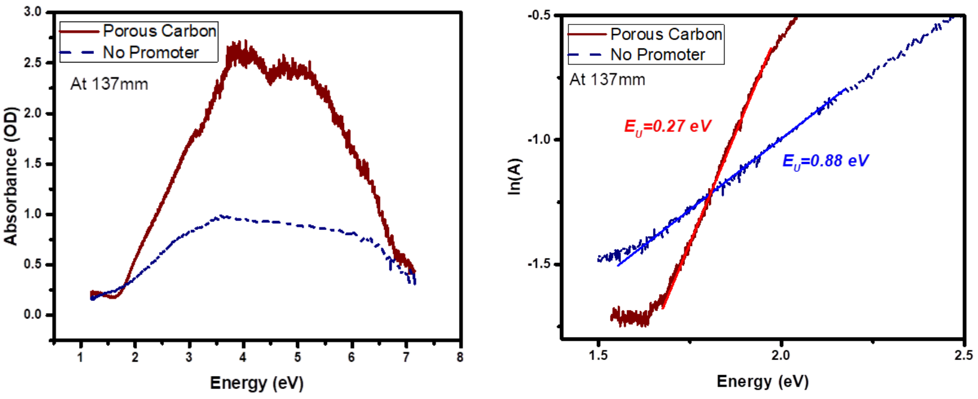

(a) (b)

Figure 4.3: (a) The absorbance spectra for with/without promoter $SnSe_2$ film at 137 mm from the precursor. (b) The Urbach energy fitting for with/without promoter $SnSe_2$ film at 137 mm from the precursor. The Urbach energies for with/without promoter sample are 0.27 eV and 0.88 eV respectively.

The increase of crystalline quality and thickness can be attributed to three main possible: (1) the carbon reduce the activation energy of the reaction 2.2 that increasing the reaction rate of the $SnSe_2$ film. (2) The porous structure of porous carbon has a large surface area to make the reaction more easily and (3) the porous structure also traps the gas flow and slows the flow rate so that the precursor has more time to react and form the thicker and good quality film.

4.1.2 Raman Spectra Mpping

The Raman mapping provide us the distribution of our material and other information, such as film thickness and also crystal quality. Figure 4.4 shows the A_{1g} peak intensity mapping and the FWHM mapping and figure 4.5 gives the normalized and averaged Raman spectra around the position of 137 mm from the precursor.

The intensity of the A_{1g} peak and the position of the E_g peaks give us information on the film thickness. Focus on the region around 137 mm from the precursor. In figure 4.4 we may see that the A_{1g} intensity of promoter assisted sample is higher than that of no promoter one, which is matching to the absorption mapping, and the A_{1g} intensity is also decaying in the interval of 140 mm to 150 mm. Meanwhile, the peak FWHM also shows more bad crystals in the low-temperature region for the no promoter-assisted case. Which is also matching the absorption and the

doi:10.6342/NTU202301860

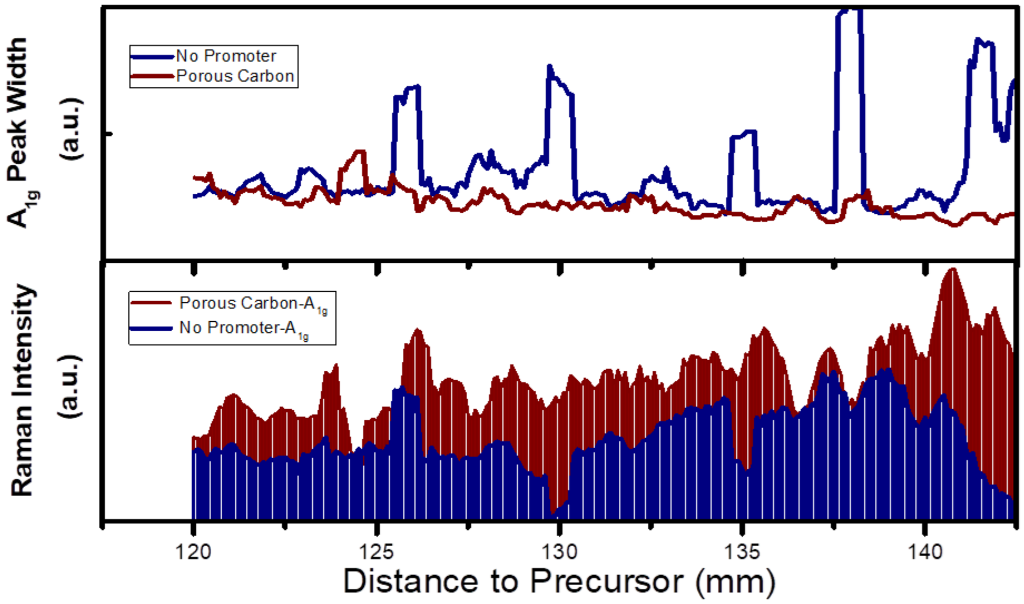

Figure 4.4: The bottom plot is the Raman mapping of A_{1g} peak for with/without promoter samples. The top plot is the FWHM of the A_{1g} peak.

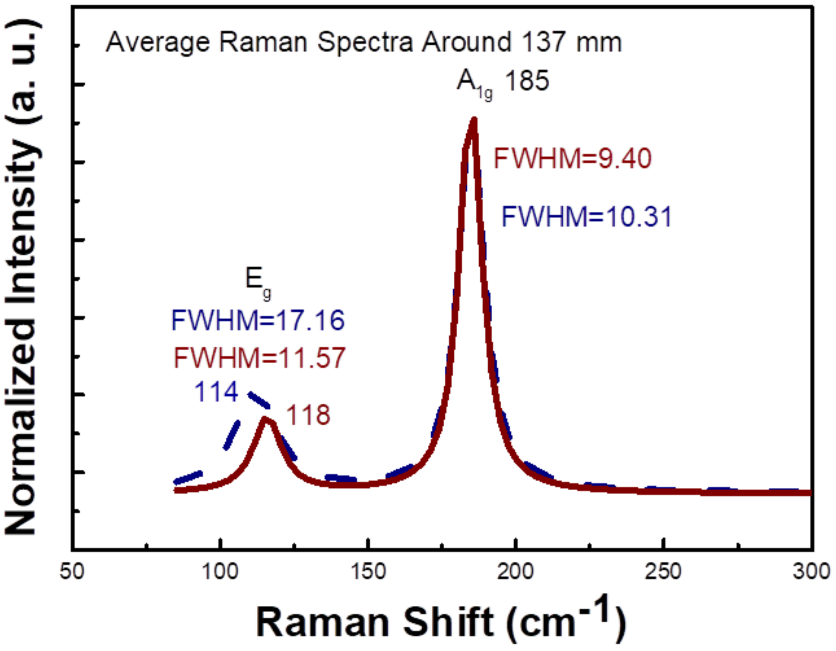

Figure 4.5: The normalized and averaged Raman spectra around the position of 137 mm from the precursor.

Urbach energy mapping.

Figure 4.5 supports that the thickness of promoter-assisted $SnSe_2$ film is thicker than no promoter one and the quality of the crystal is also better than no promoter one. The E_g peak is located in 112 cm^{-1} to 118 cm^{-1}, which indicates the phase of $SnSe_2$ is 2H phase. The E_g peak of no promoter assisted one has shifted to 114 cm^{-1} and the decreased shifting of E_g position points out the thinner thickness of the film. [31]. The shifting of the E_g peak can be attributable to surface effects and inter- and inner-layer couplings.[69] The FWHM of both peaks for the promoter-assisted $SnSe_2$ are smaller than that of no promoter-assisted one, which also reveals the better crystal quality of promoter-assisted $SnSe_2$ sample.

The intensity ratio of A_{1g} and E_g peak for no promoter assisted $SnSe_2$ film in figure 4.5 is smaller than that of promoter-assisted one. Which indicates that the A_{1g} intensity is higher for the promoter assisted $SnSe_2$ and a higher A_{1g} intensity corresponds to a thicker thickness due to the increasing of the van der Waals forces. The A_{1g} mode is reflecting the out-plane vibration, thicker film has more layers so that it makes the van der Waals forces increasing and the correspond Raman peak also intensity increasing.[31]

doi:10.6342/NTU202301860

4.1.3 Stoichiometric Composition

In this section, we give the stoichiometric composition of the synthesized sample. We mainly use two kinds of examinations to find the stoichiometric composition, EDX and XPS.

- **SEM & EDX**

The SEM image in figure 4.6 shows the polycrystalline structure of the $SnSe_2$ film, we may observe many gaps in the image.

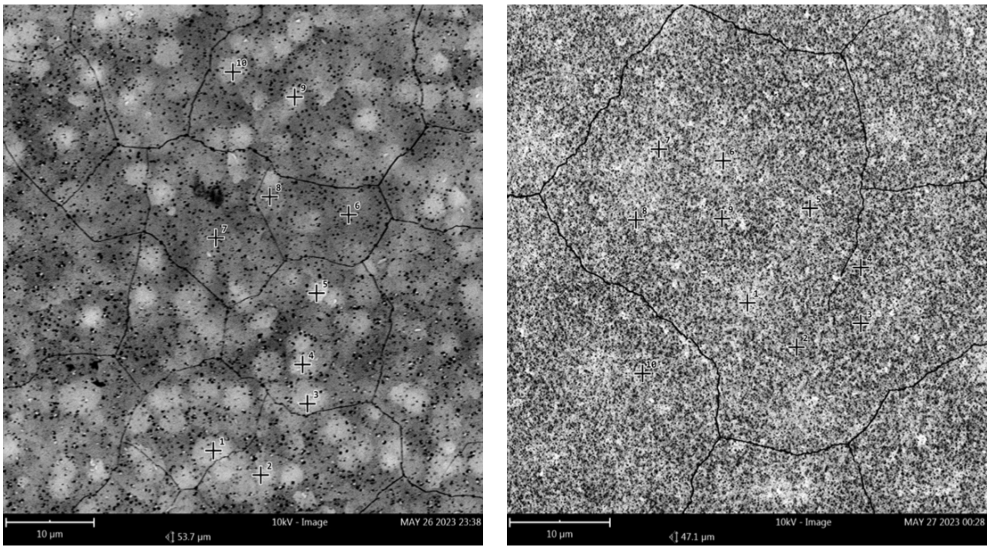

(a) (b)

Figure 4.6: (a) The SEM image for the porous carbon assisted growth $SnSe_2$ sample. (b) The SEM image for the no promoter assisted growth $SnSe_2$ sample.

Figure 4.6(a) shows that the porous carbon assisted sample has many thin flakes on the top of the film. According to the EDX examination, those flakes have a

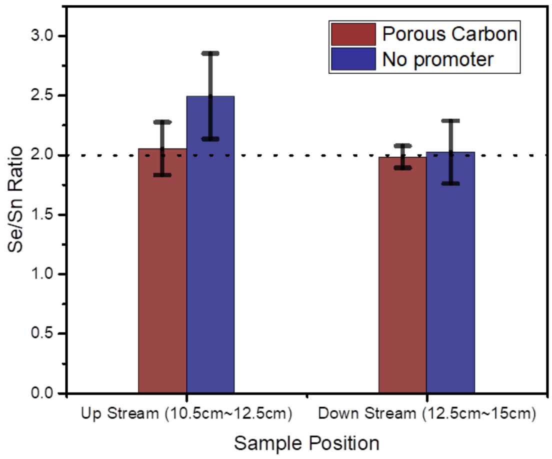

Figure 4.7: The tin/selenium atomic ratio of the two regions of the sample. The upstream is where far from the promoter and has a higher temperature, the downstream region is near the promoter and has more effect from the promoter. The promoter assisted sample has less standard deviation which may be attributed to higher crystal quality.

ratio of Se:Sn of 2.01:1 and a large size (near 2μm to 5μm wide and long), they are $SnSe_2$ flakes. In figure 4.6(b), the surface of the $SnSe_2$ film covered many tiny crystals (a few hungers nanometers) and those crystals are growing vertically. The EDX shows they have Se:Sn ratio of 2.3:1, it shows that some selenium was not react.

Figure 4.7 shows the average atomic ratio of tin and selenium. The Se/Sn ratio and the standard deviation for with/without promoter-assisted $SnSe_2$ samples in the upstream region (10.5 cm to 12.5 cm) are worse than that in the downstream region. The no promoter sample in the upstream region has a higher Se/Sn ratio, which may be due to non-reacted selenium or $SnSe_{2+x}$ crystal. Let's focus on the downstream region, the Se/Sn ratio is close to 2.0 for both samples, which gives the stoichiometric composition of $SnSe_2$. However, the without promoter-assisted sample shows a higher standard deviation than the promoter-assisted sample. That provides a shred of evidence to prove that porous carbon can improve crystal quality.

- **XPS**

Figure 4.8(a) and figure 4.8(b) are the XPS spectrum of selenium and tin for the porous carbon-assisted $SnSe_2$. In figure 4.8(a), the XPS spectrum shows two main peaks for Sn-Se bonds: Se $3d_{3/2}$, at 54.60eV, and Se $3d_{5/2}$, at 53.70 eV. The separation between the two peaks is 0.9 eV.[31] There is the other peak in this spectrum, the peak belongs to the non-reacted selenium,[70] which is corresponds to the deviation error of the EDX. In Figure 4.8(b), the XPS shows two main peaks, at 494.94 eV and 484.50 eV, correspond to Sn $3d_{3/2}$ and Sn $3d_{5/2}$ respectively. Those peaks belong to the Sn-Se bond.[71]

Figure 4.8(c) and figure 4.8(d) are the XPS spectrum of selenium and tin for the no promoter-assisted $SnSe_2$. In figure 4.8(c), the XPS spectrum shows two

doi:10.6342/NTU202301860

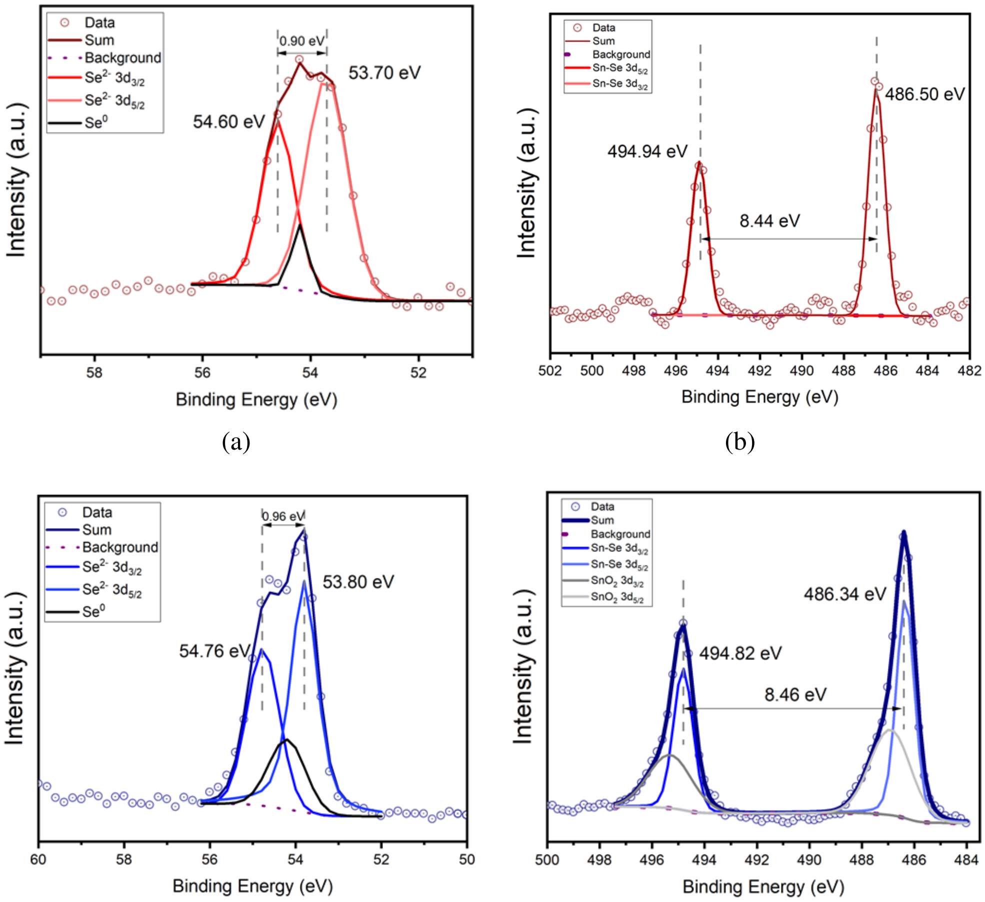

(a) (b)

(c) (d)

Figure 4.8: (a) and (b) are the bonding energy of selenium and tin for the porous carbon-assisted $SnSe_2$ film. (c) and (d) are the bonding energy of selenium and tin for the no promoter-assisted $SnSe_2$ film.

main peaks for Sn-Se bonds: Se $3d_{3/2}$, at 54.76 eV, and Se $3d_{5/2}$, at 53.80 eV. The separation between the two peaks is 0.96 eV. There also exists the peak belongs to the non-reacted selenium. In Figure 4.8(d), the XPS shows two main peak groups, one group at around 495 eV and the other group at around 484 eV, the two peak groups correspond to Sn $3d_{3/2}$ and Sn $3d_{5/2}$ respectively. The peaks at 495.8 eV and 487.2 eV can be attributed to the Sn-O bonds, the formation of SnO_2 may be due to the oxidation of the sample.[72] The peaks at 494.82 eV and 486.34 eV belong to the Sn-Se bond.[71]

From the ratio of peak area/RSF correlation of Sn-Se bonds in tin and selenium XPS spectrum, the stoichiometric composition for the porous carbon assisted sample is Sn:Se=1:1.98; while for the no promoter assisted sample, the Sn:Se ratio is 1:1.94. Both of them are close to 1:2, which is matched the stoichiometric composition of $SnSe_2$.

4.1.4 AFM Characterization

The AFM image gives us the morphology of the film grown on the quartz slides.

The SEM image is hard to see the detail of the film structure because the $SnSe_2$ sample and fused quartz substrate are not good conductors. When we magnified

doi:10.6342/NTU202301860

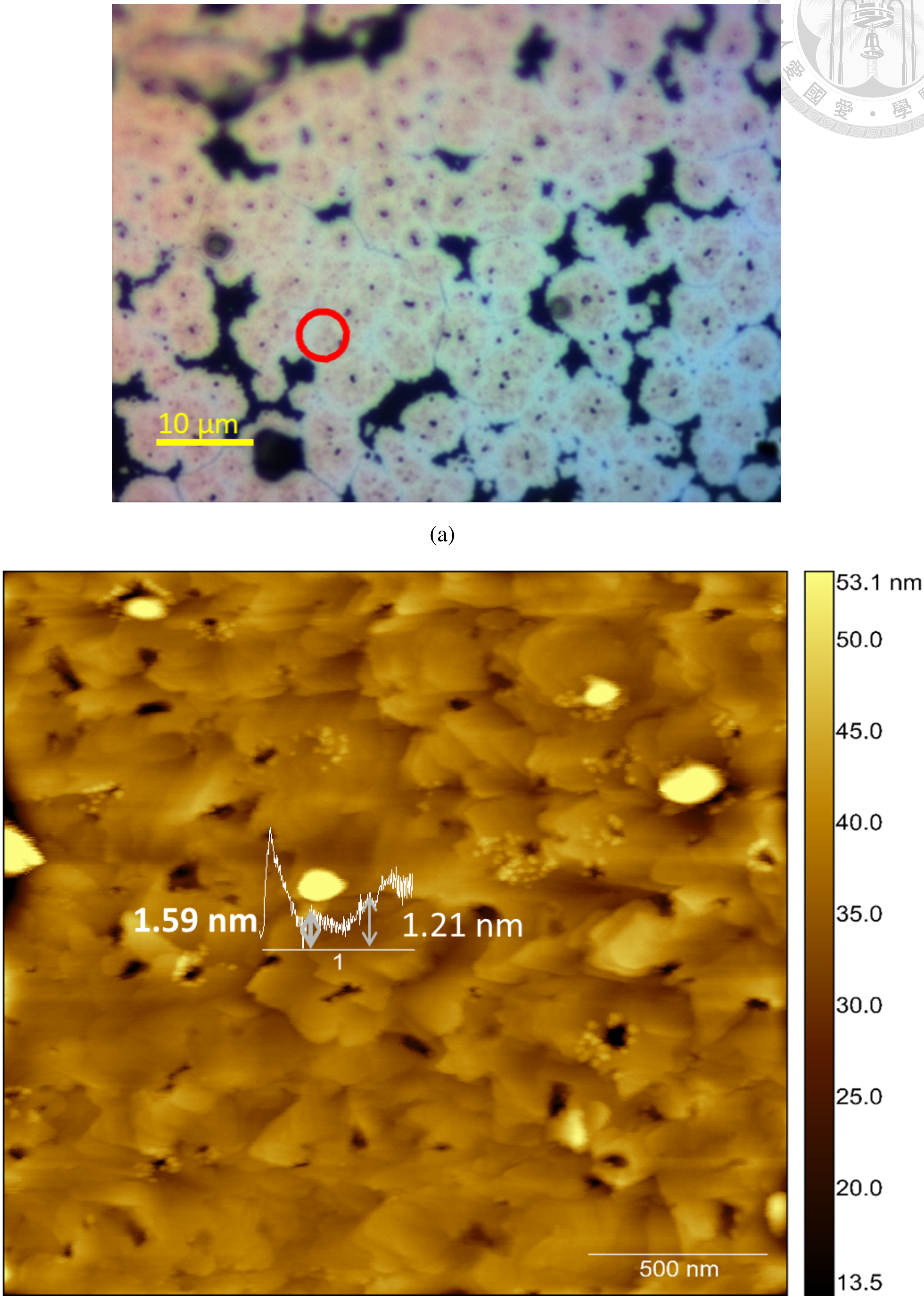

(a)

(b)

Figure 4.9: (a) The optical microscopic image of the low coverage $SnSe_2$ film grown on the fused quartz. (b) The AFM image of the $SnSe_2$ film.

the scan region, the charges accumulate on the sample surface and we can get a good image in this condition. Even we coating Pt for a few nanometer still couldn't solve this problem. To get a high-quality morphology image, we have to use AFM to scan the surface. We chose a low-coverage area to scan so that we may avoid the vertical flakes on the surface of the film interfering with the scan.

Figure 4.9(a) shows the optical microscopic image of the low coverage $SnSe_2$ film grown on the fused quartz, and figure 4.9(b) shows the AFM image of the $SnSe_2$ film in the red circle region in figure 4.9(a). The AFM image reveals the morphology of the $SnSe_2$ film is composed of many small $SnSe_2$ nanoflakes. The thickness of each flake is around 1.2 nm to 1.6 nm, which corresponds to the thickness of a few layers $SnSe_2$.[35] Other AFM analysis shows the film thickness near the porous carbon is around 40 nm to 100 nm; compare to the no promoter-assisted sample, the film thickness is only 30 nm to 80 nm. Figure 4.10 shows the thickness of $SnSe_2$ film grown on a fused quartz slide, the thickness of the film is 70 nm. This result is also matching the mapping result in the previous sections.

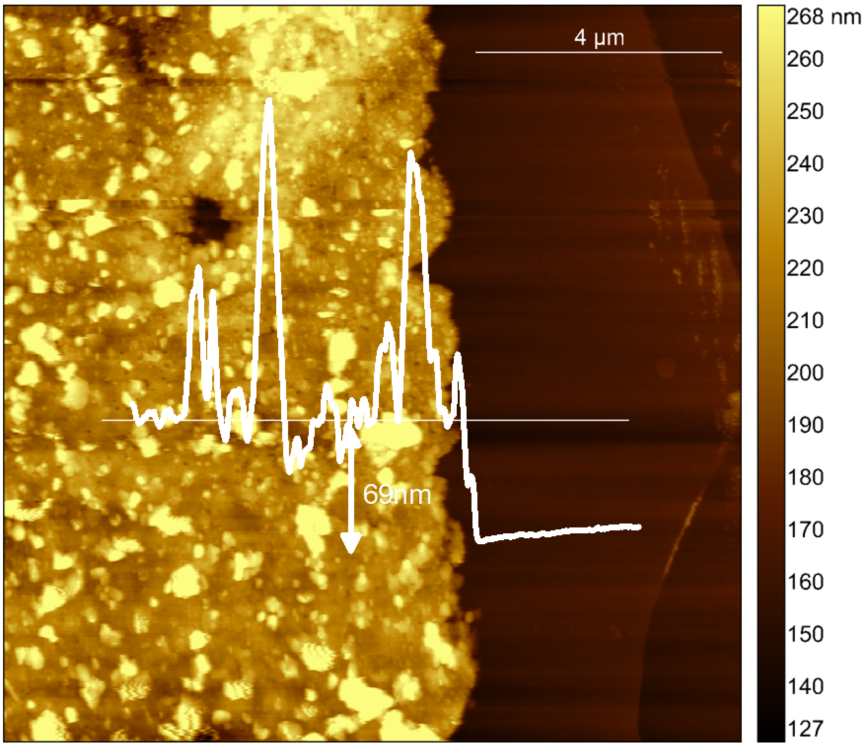

Figure 4.10: The AFM image shows the thickness of $SnSe_2$ film grown on the quartz substrate is approximately 70 nm.

4.1.5 SAED

Figure 4.11(a) and 4.11(b) shows the selected area electron diffraction, SAED, pattern for without/with promoter assisted $SnSe_2$ film. The diffraction pattern shows a good crystalline quality for the $SnSe_2$ samples.

The d-spacing formula for hexagonal lattice is:

$$\frac{1}{d} = \frac{4}{3}(\frac{h^2 + hk + k^2}{a^2}) + \frac{l^2}{c^2} \tag{4.1}$$

where $1/d$ is the d-spacing length in unit of nm^{-1}, $\langle hlk \rangle$ is the plane orientation and a, c are lattice constants. For $SnSe_2$, the lattice constants are: $a = 3.81\ \mathring{A}$, $c = 6.14\ \mathring{A}$. Here, we show two planes, $\langle 100 \rangle$ ($1/d = 3.031\ nm^{-1}$) and $\langle 110 \rangle$ ($1/d = 5.249\ nm^{-1}$), of the $SnSe_2$ film.

4.2 Applications

After we checked the characterizations of the synthesized $SnSe_2$, we are going to find their applications of them. Previous research has investigated the thermoelectric properties of the porous carbon-assisted $SnSe_2$ film.[2] Those thermoelectric properties include the Seebeck coefficient, the ZT value, and thermal conductivity.

doi:10.6342/NTU202301860

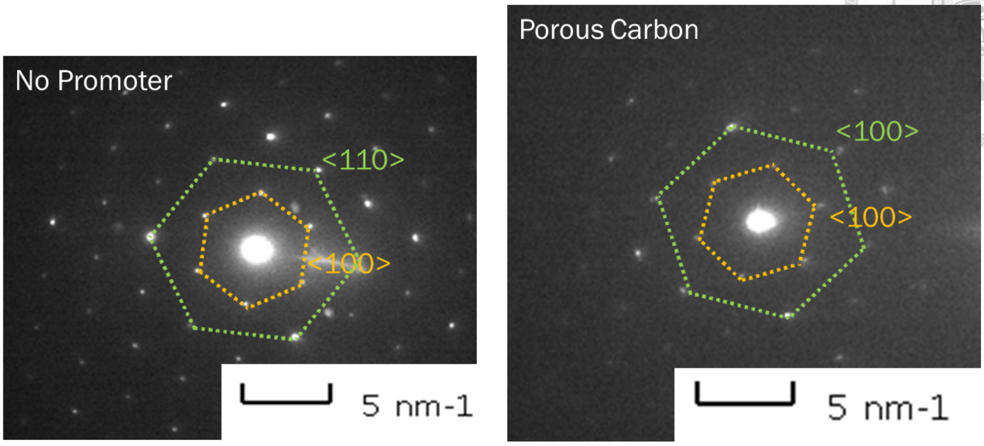

(a) (b)

Figure 4.11: The SAED diffraction pattern of (a) the no promoter assisted $SnSe_2$ and (b) the promoter assisted $SnSe_2$ film.

In this work, we will focus on the applications of the photodetector and the future possible application development goal: flexible device, for instance, strain gauge.

4.2.1 Thermoelectric Properties of The Promoter Assisted $SnSe_2$ Film

Figure 4.12(a) shows a negative Seebeck coefficient with value $-131.93\ \mu V/K$, which reveals the n-type nature of the synthesized $SnSe_2$ film.[73] Figure 4.12(b) shows the ZT value equals to 0.543, which is measured by the Harman method.[74] We may see the fast-decreasing region in figure 4.12(b) has two segments, the top one is the voltage due to Ohm's law, V_R, and the bottom one is due to the thermal

doi:10.6342/NTU202301860

reaction, V_{th}. The ZT value can be calculated by Harman method:

$$ZT = \frac{V_{th}}{V_R}. \tag{4.2}$$

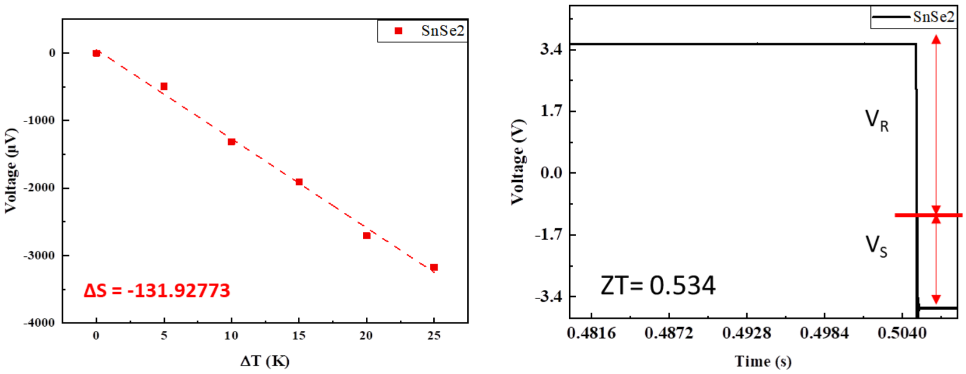

(a) (b)

Figure 4.12: (a) The Seebeck coefficient of porous carbon assisted $SnSe_2$. (b) The ZT value of the $SnSe_2$ film measured by the Harman method.[2]

The thermal conductivity, κ, can be obtained by using LASER to heating the $SnSe_2$ sample and using the relation:

$$\kappa = \frac{\chi_T W}{2tL\chi_p} \tag{4.3}$$

where χ_T and χ_p are coefficient of temperature and power respectively, t is the thickness of the film, W is the width of the film and L is the length of the film. The calculated κ is 5.83 W/mK.[2]

4.2.2 I-V Measurements

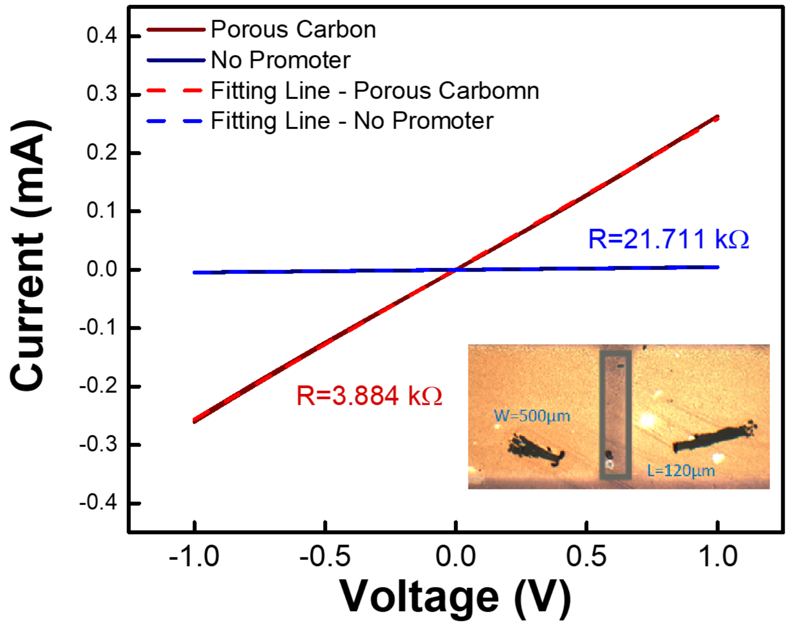

Figure 4.13: The current-voltage measurement of with/without promoter samples. The inset image is the dimension of the electrodes and material coverage area.

The current-voltage measurement, shown in figure 4.13, shows the resistances of the $SnSe_2$ films with/without promoter assisted are 3.884 kΩ and 21.711 kΩ respectively. From the inset image in figure 4.13, the material area is 120 μm × 500 μm, and by AFM measurement the thickness of the film is approximately 70 nm. According to eq.3.15, the conductivity of the with/without promoter assisted

doi:10.6342/NTU202301860

$SnSe_2$ films are 883 S/m and 156 S/m respectively. The better crystalline quality of the promoter-assisted one has better conductivity. Here, we set $l = 120\ \mu m$, $w = 500\ \mu m$ and $t = 70\ nm$.

We also trying to measure the mobility via two kinds of method: the van der Pauw method and liquid-ion gate method.

First, from the van der Pauw method, the sheet resistance of the sample is around 90 kΩ to 120 kΩ and the calculated carrier mobility is in the range of 12 cm^2/Vs to 104 cm^2/Vs for the porous carbon promoted $SnSe_2$ film; the sheet resistance of the sample is around 110 kΩ to 130 kΩ and the calculated carrier mobility is in the range of 14 cm^2/Vs to 57 cm^2/Vs for the no promoter assisted $SnSe_2$ film. The measured sheet resistances are very large and the calculated carrier mobilities are very unstable, this instability may be attributed to the bad contact of electrodes and probe or the discontinuous of the film. To avoid the disturbance we mention above, we use another way to get carrier mobilities. That is the liquid-ion gate method.

To measure mobility by the liquid-ion gate method, we need to make a MOSFET device on our sample. We made two electrodes on the $SnSe_2$ film as drain and source. Then coating a layer of photo-resistance on the sample. Next, remove the photo-resistance on the top of the channel and electrode pads for landing the probes. The device image is shown in figure 4.14(a), the light rectangular region is the channel without photo-resistance. The channel size is $W = 226\ \mu m$ and $L = 20\ \mu m$. The measurement set-up is shown in figure 4.14(b). We dropped some PEO:LiClO$_4$ (20:1 wt) solution on the channel as the gate, the solution was contacting the SnSe$_2$ film in the region without photo-resistance.

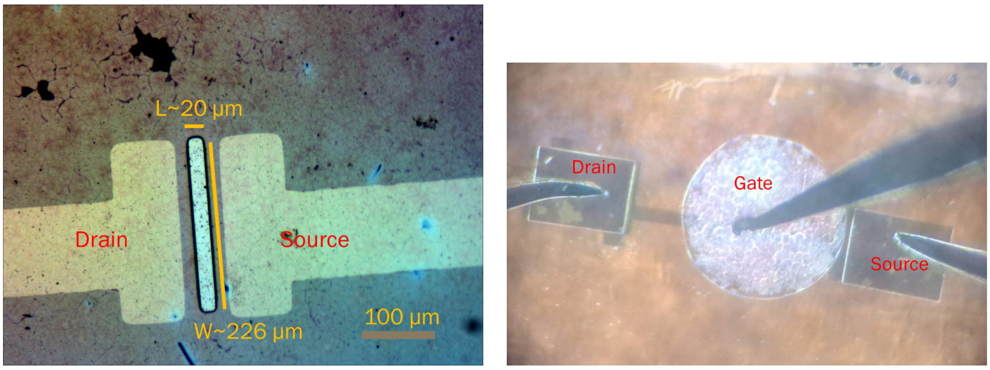

(a) (b)

Figure 4.14: (a) The OM picture of the MOSFET device. The whole region in this image were covered photo-resistance except the light rectangular region. (b) The I-V measurement set-up for the liquid-ion gate.

The I-V curve of the liquid-ion gate for with/without promoter-assisted SnSe$_2$ films are shown in figure 4.16(a) and figure 4.16(b) respectively. The curve can be separated into three parts corresponding to three work regions of a MOSFET: (1) Cutoff region, (2) Triod region, and (3) Saturation region. We fixed the voltage between the drain and source of the MOSFET, V_{DS}, and changed the voltage

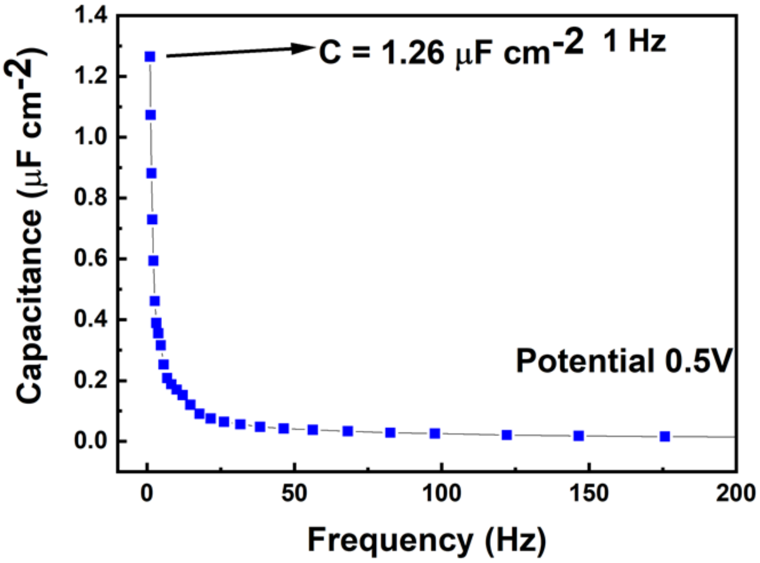

Figure 4.15: The frequency-depend capacitance for the PEO:LiClO$_4$ solution. The capacitance at 1 Hz is 1.26 $\mu F/cm^2$.

between the gate and source of the MOSFET, V_{GS}, then measure the current pass through drain and source, I_{DS}. The slopes of the triode region are positive and the saturation regions are at positive V_{GS} region for both with/without promoter-assisted samples, which shows the synthesized films are n-type semiconductors just like SnSe$_2$.

Let's focusing on the triode region. The I_{DS} in the triode region of a n-MOSFET is:

$$I_{DS} = k_n((V_{GS} - V_t)V_{DS} - \frac{V_{DS}^2}{2}) \tag{4.4}$$

doi:10.6342/NTU202301860

where V_t is the threshold voltage, which is a constant; and

$$k_n = \mu_n C_{ox}(\frac{W}{L}) \tag{4.5}$$

where μ_n is the carrier mobility, C_{ox} is the unit capacitance of the oxidation layer, W and L are the width and length of the channel of the MOSFET.

Since the $V_{DS} = 1\ V$ and V_t are constant, eq.(4.4) can be rewrite in the form:

$$I_{DS} = k_n V_{GS} + k \tag{4.6}$$

where k is a constant. We can find k_n form the slope of linear fitting of the triode region.

The k_n values for with/without promoter assisted $SnSe_2$ are 10 $\mu A/V^2$ and 2.20 $\mu A/V^2$ respectively. And from figure 4.14(a), the aspect ration W/L is approximately 11.0; also from figure 4.15, the C_{ox} of the PEO:$LiClO_4$ at low frequency is 1.26 $\mu F/cm^2$. The mobilities of the with/without promoter-assisted $SnSe_2$ are 0.72 cm^2/Vs and 0.16 cm^2/Vs respectively. The promoter-assisted $SnSe_2$ film has 4.54 times better mobility than no promoter-assisted one. It may

doi:10.6342/NTU202301860

due to the better crystal quality or thicker film thickness. The low mobility of the $SnSe_2$ may be attributed to the layer-by-layer structure, the gaps between layers create more barrage for the transfer of the free electrons.

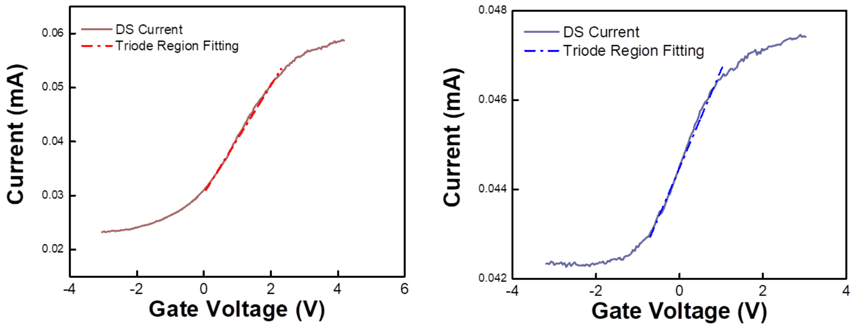

(a) (b)

Figure 4.16: (a) The I-V curve for the liquid-ion gate of promoter assisted $SnSe_2$. (b) The I-V curve for the liquid-ion gate of no promoter assisted $SnSe_2$.

The summary of the electric properties of with/without promoter assisted $SnSe_2$ films are listed in table.4.1.

Table 4.1: The measured electric properties of with/without promoter assisted $SnSe_2$ film.

	Without Promoter	With Promoter
Semiconductor Type	n-type	n-type
Conductivity (S/m)	156	883
Mobility (cm^2/Vs)	0.72	0.16

4.2.3 Photoresponse and Figures of Merit

In this part, we demonstrate the application of the $SnSe_2$ film on the photo detector.

Figure 4.17 shows the photocurrents of with/without promoter $SnSe_2$ film at different power density levels, and figure 4.18 shows the I-V curve of the $SnSe_2$ with/without promoter assisted for dark and the incident power density at 108 mW/cm^2. We can see that the photocurrent of promoter-assisted $SnSe_2$ film is more than 60 times larger than that of no promoter-assisted one. There are many factors to affect the magnitude of photocurrent, but the most apparent one is the conductivity. From the previous section, we have known that the conductivity of promoter-assisted $SnSe_2$ is much better than that of no promoter one due to a better crystalline quality and thicker thickness.

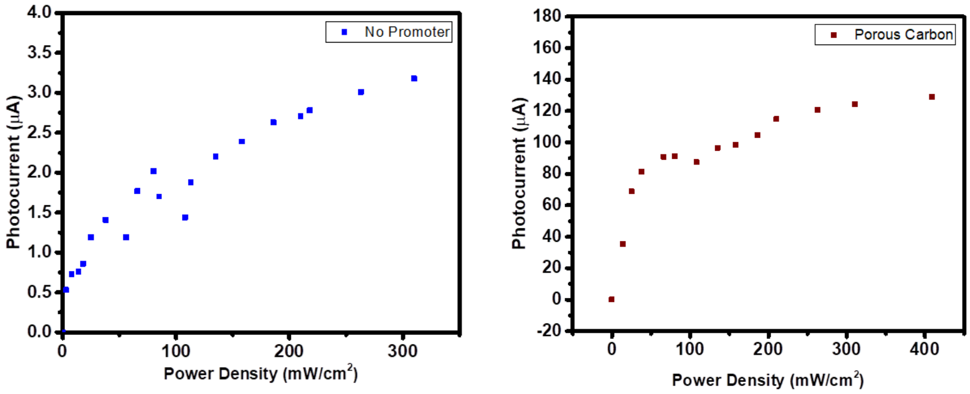

(a) (b)

Figure 4.17: The photocurrent v.s. incident light power density of no promoter assisted $SnSe_2$ film, (a), and promoter assisted $SnSe_2$ film, (b).

doi:10.6342/NTU202301860

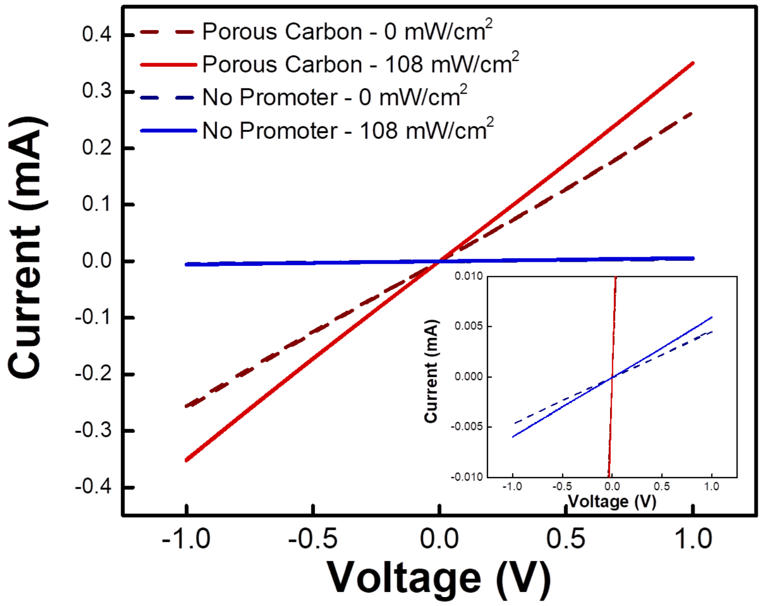

Figure 4.18: The I-V curve of with/without promoter assisted $SnSe_2$ film for dark and the incident power density at 108 mW/cm^2. The inset plot is the magnified plot for the no promoter assisted $SnSe_2$ film.

Figure 4.19(a) is the photo-response on-off test for the $SnSe_2$ films, biased at 1V; figure 4.19(b) and 4.19(c) shows the rise time and decay time for the on-off current change. We normalized the photocurrent so that we can compare the rise time and decay time more efficiently and the response time is defined as the time between 10% to 90% height of the on or off edge. The rise time and decay time for the no promoter-assisted $SnSe_2$ sample are 77.70 ms and 62.40 ms respectively; while the rise time and decay time for the promoter-assisted sample are only 7.11 ms and 22.30 ms. The rise time and decay time of the promoter-assisted $SnSe_2$ sample are shorter than that of the no promoter-assisted one. From eq.(1.1), we may attribute the shorter response time to the higher mobility.

In figure 4.18 we have seen that as bias voltage equals to 1V and incident light power density equals to 108 mW/cm^2 at 532 nm, the photocurrents of the with/without promoter samples are 263 μA/4.50 μA, and the effective device area is also 500 $\mu m \times$ 120 μm, by eq.(1.3), we have the responsivity, $\mathscr{R} = 4.29\ A/W$ and $0.09\ A/W$ for the sample with/without promoter respectively. The EQE and detectivity can also be found by eq.(1.4) and eq.(1.5). The EQE for with/without promoter assisted sample are 1002% / 21.02%, and the detectivities of them are 11.5G Jones / 1.84G Jones. Those figures of merit shows the promoted $SnSe_2$ has a good performance in responsivity and EQE. Table.4.2 listing the figures of merit for the with/without promoter assisted $SnSe_2$.

The good resposivity can be attributed to the good photocurrent. The photocurrent is generated by two steps (for n-type semiconductor, the main carriers are electrons): (1) Incident photons with a energy higher than the band gap of the material absorbed and excite the electrons to generate electron-hole pairs. (2) The electron-hole pairs is separated by the bias voltage, electrons and holes are moving in a opposite direction. This way to generate photocurrent is called the photoconductive effect.

doi:10.6342/NTU202301860

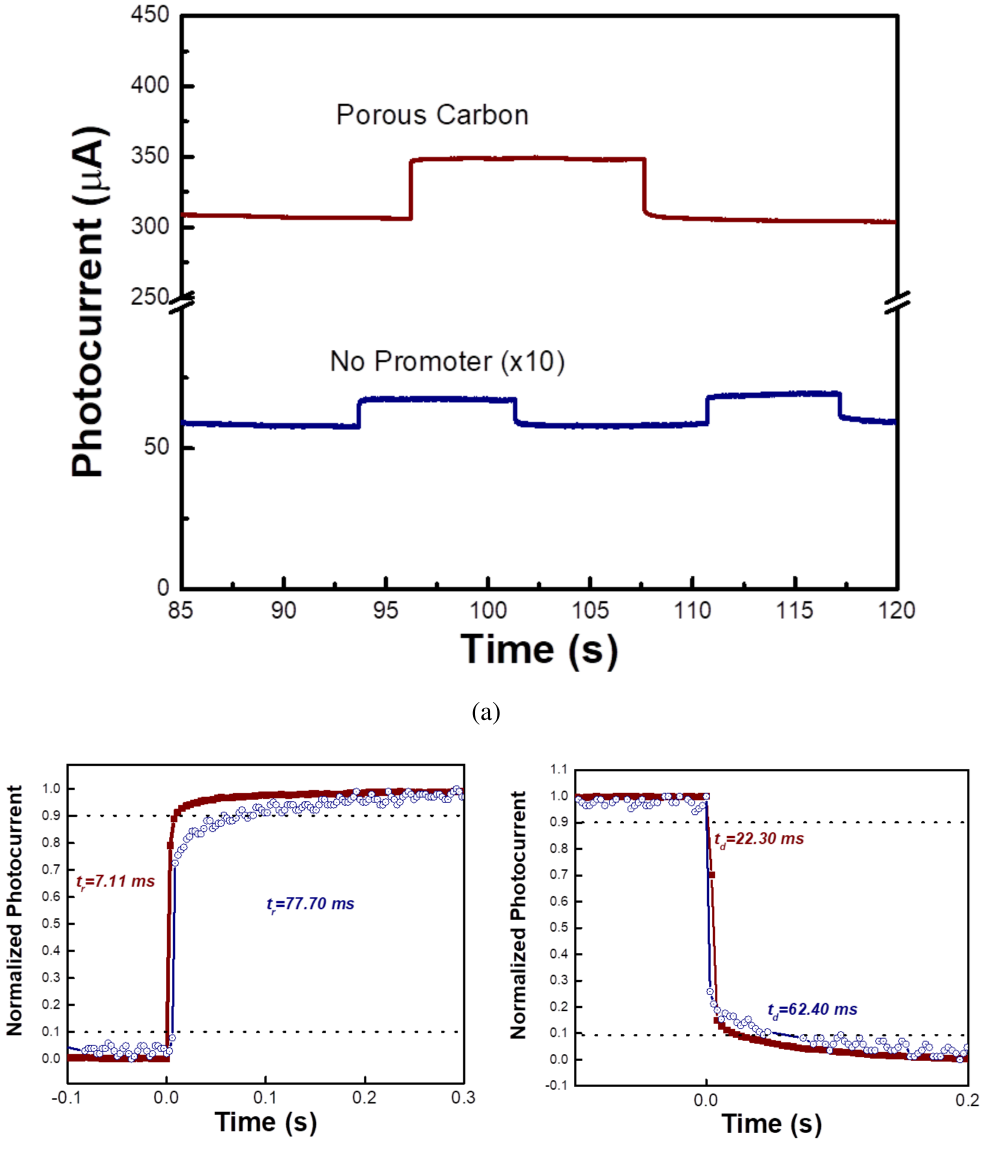

(a)

(b) (c)

Figure 4.19: (a)The on-off test for $SnSe_2$ films.(b) and (c) shows the rise time and decay time respectively.

doi:10.6342/NTU202301860

Table 4.2: The figures of merit of photodetector of with/without promoter assisted $SnSe_2$ film.

Figures of Merit	Without Promoter	With Promoter
Rise Time (ms)	77.70	7.11
Decay Time (ms)	62.40	22.30
Dark Current (μA)	4.5	263
Photocurrent* (μA)	0.76	36
On-Off Ratio	0.169	0.137
Responsivity** (A/W)	0.09	4.29
EQE (%)	21.02	1002
Detectivity** (Jones)	1.84×10^9	11.5×10^9

*Measured at $\mathscr{P}$ =14 mW/cm^2 and $\lambda = 532\ nm$.

**The device area is $6 \times 10^{-4}\ cm^2$.

Since our sample has some trap states generated by the defects, those trap states also affect the photocurrent and lifetime. For more trap state material, electrons are trapped in the localized states located at defects and/or at surface adsorbates. Consequently, one type of carrier is transferred to the channel, leaving oppositely-charged carriers trapped in the surface adsorbates or traps. These trapped carriers act as local gates and effectively modulate the conductance of the semiconductor due to electrostatic interactions. The carriers in the semiconductor can recirculate many times during the lifetime of the trapped carriers, leading to a high gain. This way to generate photocurrent is called the photogating effect, a special case of photoconductive effect.[75]. Although photodetectors with a photogating effect

doi:10.6342/NTU202301860

can have a higher on-off ratio than photoconductors, they usually have a slower response speed.

In this work, we may observe that the no promoter-assisted $SnSe_2$ has more defect states than that of promoter-assisted $SnSe_2$ so they have a longer reaction time and a higher on-off ratio.

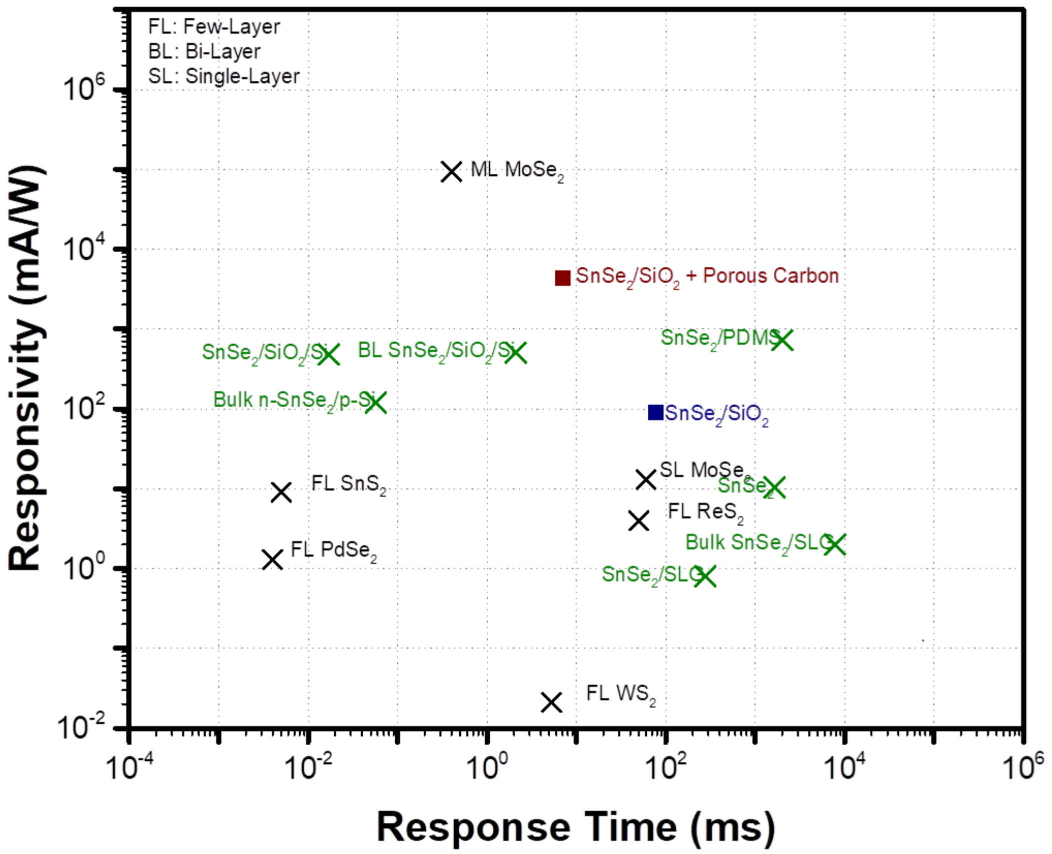

Figure 4.20: Responsivity v.s. response time for a large number of reported photodetector studies. $SnSe_2$ in this work are the navy color and the wine color squares.[3, 4, 5, 6, 7, 8, 9, 10, 11, 12, 13, 14]

Figure 4.20 shows the responsivity v.s. response time for a large number of reported photodetector studies. The porous carbon-assisted $SnSe_2$ film in this work has a great responsivity than many $SnSe_2$ in other reports. In this work, the response time is longer than in some reports, it's might due to some reasons: (1) The low mobility of our sample. In other works, they use a single-layer or bi-layer $SnSe_2$ flake, but our $SnSe_2$ film is polycrystalline structure so that the grain boundaries reduce the carrier mobility. (2) The photodetector channel length in this work is much longer than other works, longer distance contains more gaps or grain boundaries in the sample so that we have a longer rise time.

Figure 4.21 shows the responsivity v.s. synthesis temperature for $SnSe_2$ in other works and our works, we have the best responsivity at the lowest synthesis temperature. We may see that the no promoter assisted $SnSe_2$ sample at low temperature has a worse responsivity than many $SnSe_2$ in other works. It's not a surprising result because the responsivity is related to the photocurrent and the photocurrent is related to electronic conductivity. At low temperatures, it's hard to synthesize $SnSe_2$ with good quality.

However, once we put porous carbon to assist the synthesis process at low temperatures, the crystal quality is increasing and the conductivity also increases. The responsivity is increasing more than 47 times and is also better than most

doi:10.6342/NTU202301860

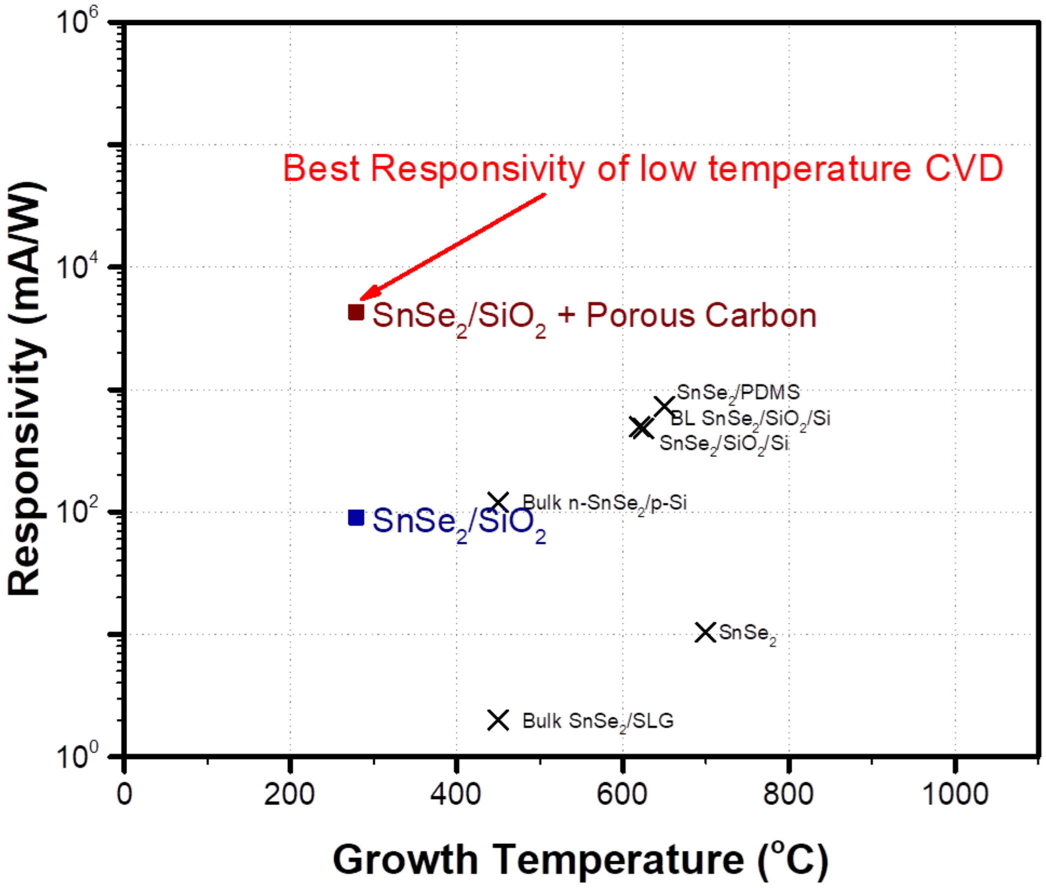

Figure 4.21: Responsivity v.s. synthesis temperature for $SnSe_2$ in other works and our works.[9, 10, 11, 12, 13, 14]

doi:10.6342/NTU202301860

of the reported $SnSe_2$ samples. This result gives us more confidence that the porous carbon promoter is useful for low-temperature synthesizing $SnSe_2$ and also enhances its quality and we may trying to use the new synthesis method to make $SnSe_2$ grow on other flexible substrates at low temperature.

4.2.4 Out looks - Applications in Strain Gauges

In the out-look application part, we have made $SnSe_2$ grown on a flexible substrate, Willow glass, via the new porous carbon assisted method. In figure 4.22 we demonstrate the strain gauge performance. The gage factor for the $SnSe_2$/Willow glass is 13.46.

The changing of resistance with strain may be attributed to the structure of the film. Since the $SnSe_2$ film is composed of many stacked nano-flakes, as we bend the substrate, the gap between those flakes would be enlarged. That enlarged gap makes more barriers for the transfer of electrons and then increases the resistance.

In the future, we may be trying to improve the CVD synthesis process to make $SnSe_2$ grow on other flexible substrates, such as polyamide (PA, M.P.=180^{o}C to 210^{o}C), Polyimide (PA, M.P.=470^{o}C) and poly(ethyl benzene-1,4-dicarboxylate) (PET, M.P.=260^{o}C), at low temperature by using the porous carbon as a promoter.

doi:10.6342/NTU202301860

The good thermoelectric properties of the $SnSe_2$ have many applications, like a flexible self-power photodetector or flexible solar cell, etc.

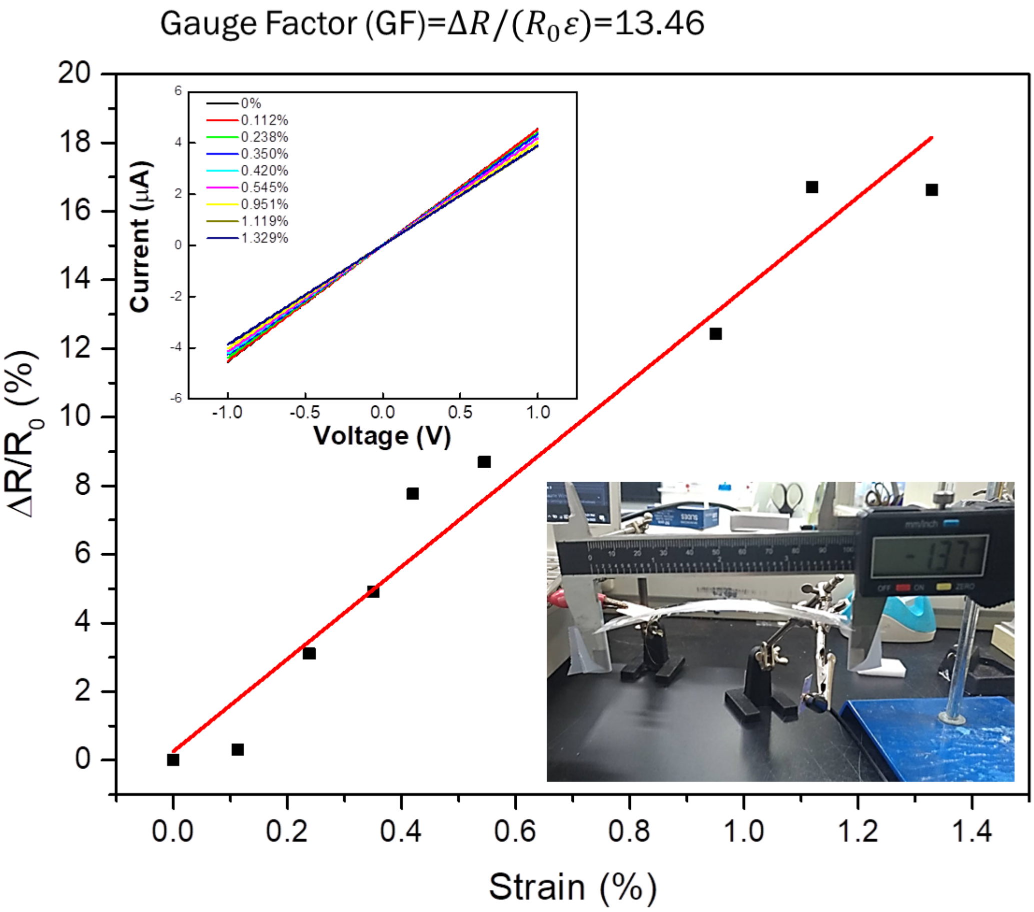

Figure 4.22: The changing of resistance v.s. strain plot. The inset image is the schematic diagram of the measurement of the gauge factor.

doi:10.6342/NTU202301860

doi:10.6342/NTU202301860

Chapter 5

Conclusion

In this work, we provide a new way to synthesize $SnSe_2$ at low temperatures by CVD method. We used a porous carbon, which is obtained by dehydrating the melamine sponge, as a promoter to assist $SnSe_2$ grow on a quartz slide at a low temperature.

The stoichiometric analysis, EDX and XPS, shows the ratio of Sn:Se is close to 1:2, which is corresponding to $SnSe_2$; the Raman mapping and absorption spectra mapping show the trends that at the low-temperature region, our porous carbon promoter is making $SnSe_2$ grown on the fused quartz substrate thicker and better crystalline quality. The Raman spectra also show the $SnSe_2$ is 2H phase. Also, the promoter-assisted synthesized $SnSe_2$ has good thermoelectric properties and

doi:10.6342/NTU202301860

enhanced performance in the photodetector. For the thermoelectric properties part, the Seebeck coefficient is -131.93 $\mu V/K$ and the ZT value is 0.534. For the photodetector part, the responsivity of porous carbon-assisted $SnSe_2$ has 48 times higher than that of no promoter-assisted one. The high responsivity may be attributed to the low mobility due to the stacked flake structure and trap states in the material.

In future applications, we may try to make $SnSe_2$ grow on other amorphous, low melting points and flexible substrates by using this new method to make more wearable devices. This new method has many potential waiting for us to reveal.

doi:10.6342/NTU202301860

Reference

[1] C. V. Raman and K. S. Krishnan, “The negative absorption of radiation,” *Nature*, vol. 122, no. 3062, pp. 12–13, 1928. x, 40

[2] C. Chun-Lin, “Preparation and thermoelectric properties of porous graphene-tin diselenide heterostructures,” Master’s thesis, Feng Chia University, Taiwan, 2022. xiii, 6, 83, 85, 86

[3] Z. Yin, H. Li, H. Li, L. Jiang, Y. Shi, Y. Sun, G. Lu, Q. Zhang, X. Chen, and H. Zhang, “Single-Layer MoS2 Phototransistors,” *ACS Nano*, vol. 6, no. 1, pp. 74–80, 2012, pMID: 22165908. [Online]. Available: https://doi.org/10.1021/nn2024557 xiii, 97

[4] Lopez-Sanchez, “Ultrasensitive photodetectors based on monolayer MoS$_2$.” *Nature Nanotech*, vol. 8, pp. 497–501, 2013. xiii, 97

[5] K. J. Hong X, “Ultrafast charge transfer in atomically thin MoS/WSheterostructures.” *Nat Nanotechnol.*, vol. 9, pp. 682–686, 2014. xiii, 97

[6] J. Xia, X. Huang, L.-Z. Liu, M. Wang, L. Wang, B. Huang, D.-D. Zhu, J.-J. Li, C.-Z. Gu, and X.-M. Meng, “CVD synthesis of large-area, highly crystalline MoSe$_2$ atomic layers on diverse substrates and application to photodetectors,” *Nanoscale*, vol. 6, pp. 8949–8955, 2014. [Online]. Available: http://dx.doi.org/10.1039/C4NR02311K xiii, 97

[7] L. Y. Hu PingAn, Wang, “Highly Responsive Ultrathin GaS Nanosheet Photodetectors on Rigid and Flexible Substrates,” *Nano Letters*, vol. 13, no. 4, pp. 1649–1654, 2013, pMID: 23465066. [Online]. Available: https://doi.org/10.1021/nl400107k xiii, 97

[8] S. R. Tamalampudi, Y.-Y. Lu, R. K. U., R. Sankar, C.-D. Liao, K. M. B., C.-H. Cheng, F. C. Chou, and Y.-T. Chen, “High Performance and Bendable Few-Layered InSe Photodetectors with Broad Spectral Response,” *Nano Letters*, vol. 14, no. 5, pp. 2800–2806, 2014, pMID: 24742243. [Online]. Available: https://doi.org/10.1021/nl500817g xiii, 97

[9] X. Zhou, L. Gan, W. Tian, Q. Zhang, S. Jin, H. Li, Y. Bando, D. Golberg, and T. Zhai, “Ultrathin $SnSe_2$ Flakes Grown by Chemical Vapor Deposition for High-Performance Photodetectors,” *Advanced Materials*, vol. 27, no. 48, pp. 8035–8041, 2015. [Online]. Available: https://onlinelibrary.wiley.com/doi/abs/10.1002/adma.201503873 xiii, 2, 6, 30, 97, 99

[10] K. K. N. Emma P. Mukhokosi, Saluru B. Krupanidhi, “Band Gap Engineering of Hexagonal $SnSe_2$ Nanostructured Thin Films for Infra-Red Photodetection,” *Scientific Reports*, vol. 7, 2017. [Online]. Available: https://doi.org/10.1038/s41598-017-15519-x xiii, xv, 3, 5, 97, 99

[11] E. P. Mukhokosi, B. Roul, S. B. Krupanidhi, and K. K. Nanda, “Toward a Fast and Highly Responsive SnSe2-Based Photodiode by Exploiting the Mobility of the Counter Semiconductor,” *ACS Applied Materials & Interfaces*, vol. 11, no. 6, pp. 6184–6194, 2019. [Online]. Available: https://doi.org/10.1021/acsami.8b16635 xiii, 97, 99

[12] P. Yu, X. Yu, W. Lu, H. Lin, L. Sun, K. Du, F. Liu, W. Fu, Q. Zeng, Z. Shen, C. Jin, Q. J. Wang, and Z. Liu, “Fast Photoresponse from 1T Tin Diselenide Atomic Layers,” *Advanced Functional Materials*,

doi:10.6342/NTU202301860

vol. 26, no. 1, pp. 137–145, 2016. [Online]. Available: https://onlinelibrary.wiley.com/doi/abs/10.1002/adfm.201503789 xiii, 97, 99

[13] J. Wu, Z. Hu, Z. Jin, S. Lei, H. Guo, K. Chatterjee, J. Zhang, Y. Yang, B. Li, Y. Liu, J. Lai, R. Vajtai, B. Yakobson, M. Tang, J. Lou, and P. M. Ajayan, "Spiral Growth of SnSe$_2$ Crystals by Chemical Vapor Deposition," *Advanced Materials Interfaces*, vol. 3, no. 16, p. 1600383, 2016. [Online]. Available: https://onlinelibrary.wiley.com/doi/abs/10.1002/admi.201600383 xiii, 97, 99

[14] M. Kumar, S. Rani, A. Pandey, K. S. Gour, S. Husale, P. Singh, and V. Singh, "Highly responsive, low-bias operated SnSe$_2$ nanostructured thin film for trap-assisted NIR photodetector," *Journal of Alloys and Compounds*, vol. 838, p. 155384, 2020. [Online]. Available: https://www.sciencedirect.com/science/article/pii/S0925838820317473 xiii, 97, 99

[15] E. P. Mukhokosi, G. V. Manohar, T. Nagao, S. B. Krupanidhi, and K. K. Nanda, "Device architecture for visible and near-infrared photodetectors based on two-dimensional snse2 and mos2: A review," *Micromachines*, vol. 11, no. 8, 2020. [Online]. Available: https://www.mdpi.com/2072-666X/11/8/750 xv, 5, 9, 13, 15

[16] R. Mas-Ballesté, C. Gómez-Navarro, J. Gómez-Herrero, and F. Zamora, "2D materials: to graphene and beyond," *Nanoscale*, vol. 3, pp. 20–30, 2011. [Online]. Available: http://dx.doi.org/10.1039/C0NR00323A 1

[17] K. S. Novoselov, D. Jiang, F. Schedin, T. J. Booth, V. V. Khotkevich, S. V. Morozov, and A. K. Geim, "Two-dimensional atomic crystals," *Proceedings of the National Academy of Sciences*, vol. 102, no. 30, pp. 10 451–10 453, 2005. [Online]. Available: https://www.pnas.org/doi/abs/10.1073/pnas.0502848102 1

[18] M. Kumar, S. Rani, Y. Singh, K. S. Gour, and V. N. Singh, "Tin-selenide as a futuristic material: properties and applications," *RSC Adv.*, vol. 11, pp. 6477–

6503, 2021. [Online]. Available: http://dx.doi.org/10.1039/D0RA09807H 1

[19] M. Yi and Z. Shen, “A review on mechanical exfoliation for the scalable production of graphene,” *J. Mater. Chem. A*, vol. 3, pp. 11 700–11 715, 2015. [Online]. Available: http://dx.doi.org/10.1039/C5TA00252D 1

[20] B. Adilbekova, Y. Lin, E. Yengel, H. Faber, G. Harrison, Y. Firdaus, A. El-Labban, D. H. Anjum, V. Tung, and T. D. Anthopoulos, “Liquid phase exfoliation of MoS_2 and WS_2 in aqueous ammonia and their application in highly efficient organic solar cells,” *J. Mater. Chem. C*, vol. 8, pp. 5259–5264, 2020. [Online]. Available: http://dx.doi.org/10.1039/D0TC00659A 1

[21] C. Huo, Z. Yan, X. Song, and H. Zeng, “2D materials via liquid exfoliation: a review on fabrication and applications,” *Science Bulletin*, vol. 60, no. 23, pp. 1994–2008, 2015. [Online]. Available: https://www.sciencedirect.com/science/article/pii/S2095927316302535 1, 28

[22] G. Olimpio, D. Farias, C.-N. Kuo, L. Ottaviano, C. S. Lue, D. W. Boukhvalov, and A. Politano, “Tin Diselenide ($SnSe_2$) Van der Waals Semiconductor: Surface Chemical Reactivity, Ambient Stability, Chemical and Optical Sensors,” *Materials*, vol. 15, no. 3, 2022. [Online]. Available: https://www.mdpi.com/1996-1944/15/3/1154 2

[23] Z. Jin, X. Li, J. T. Mullen, and K. W. Kim, “Intrinsic transport properties of electrons and holes in monolayer transition-metal dichalcogenides,” *Phys. Rev. B*, vol. 90, p. 045422, Jul 2014. [Online]. Available: https://link.aps.org/doi/10.1103/PhysRevB.90.045422 2

[24] D. Wu, C. Jia, F. Shi, L. Zeng, P. Lin, L. Dong, Z. Shi, Y. Tian, X. Li, and J. Jie, “Mixed-dimensional $PdSe_2$/SiNWA heterostructure based photovoltaic detectors for self-driven, broadband photodetection, infrared imaging and

humidity sensing," *J. Mater. Chem. A*, vol. 8, pp. 3632–3642, 2020. [Online]. Available: http://dx.doi.org/10.1039/C9TA13611H 2

[25] L. Shi, Q. Li, Y. Ouyang, and J. Wang, "Effect of illumination and se vacancies on fast oxidation of ultrathin gallium selenide," *Nanoscale*, vol. 10, pp. 12 180–12 186, 2018. [Online]. Available: http://dx.doi.org/10.1039/C8NR01533C 2

[26] C. K. Zankat, P. M. Pataniya, A. Patel, S. A. Bhakhar, S. Narayan, G. Solanki, K. Patel, V. Pathak, C. Sumesh, and P. Jha, "Self-powered photodetector based on $SnSe_2/MoSe_2$ heterostructure," *Materials Today Energy*, vol. 18, p. 100550, 2020. [Online]. Available: https://www.sciencedirect.com/science/article/pii/S2468606920301696 2

[27] J. Choi, J. Jin, I. G. Jung, J. M. Kim, H. J. Kim, and S. U. Son, "$SnSe_2$ nanoplate–graphene composites as anode materials for lithium ion batteries," *Chem. Commun.*, vol. 47, pp. 5241–5243, 2011. [Online]. Available: http://dx.doi.org/10.1039/C1CC10317B 2

[28] R. Y. Wang, M. A. Caldwell, R. G. D. Jeyasingh, S. Aloni, R. M. Shelby, H.-S. P. Wong, and D. J. Milliron, "Electronic and optical switching of solution-phase deposited $SnSe_2$ phase change memory material," *Journal of Applied Physics*, vol. 109, no. 11, p. 113506, 2011. [Online]. Available: https://doi.org/10.1063/1.3587187 2

[29] K. Saritha, A. Suryanarayana Reddy, and K. Ramakrishna Reddy, "Investigation on Optical Properties of $SnSe_2$ Thin Films Synthesized by Two – Stage Process," *Materials Today: Proceedings*, vol. 4, no. 14, pp. 12 512–12 517, 2017, 2nd International Conference on Solar Energy Photovoltaic, 17th–19th December, 2016. [Online]. Available: https://www.sciencedirect.com/science/article/pii/S221478531732059X 2

[30] F. Zhang, C. Xia, J. Zhu, B. Ahmed, H. Liang, D. B. Velusamy, U. Schwingenschlögl, and H. N. Alshareef, “$SnSe_2$ 2D Anodes for Advanced Sodium Ion Batteries,” *Advanced Energy Materials*, vol. 6, no. 22, p. 1601188, 2016. [Online]. Available: https://onlinelibrary.wiley.com/doi/abs/10.1002/aenm.201601188 3

[31] Y. Zhang, Y. Shi, M. Wu, K. Zhang, B. Man, and M. Liu, “Synthesis and Surface-Enhanced Raman Scattering of Ultrathin $SnSe_2$ Nanoflakes by Chemical Vapor Deposition,” *Nanomaterials*, vol. 8, no. 7, 2018. [Online]. Available: https://www.mdpi.com/2079-4991/8/7/515 3, 74, 77

[32] A. Shafique, A. Samad, and Y.-H. Shin, “Ultra low lattice thermal conductivity and high carrier mobility of monolayer SnS_2 and $SnSe_2$: a first principles study,” *Phys. Chem. Chem. Phys.*, vol. 19, pp. 20 677–20 683, 2017. [Online]. Available: http://dx.doi.org/10.1039/C7CP03748A 4

[33] Y.-Y. Wang, D.-R. Chen, J.-K. Wu, T.-H. Wang, C. Chuang, S.-Y. Huang, W.-P. Hsieh, M. Hofmann, Y.-H. Chang, and Y.-P. Hsieh, “Two-dimensional mechano-thermoelectric heterojunctions for self-powered strain sensors,” *Nano Letters*, vol. 21, no. 16, pp. 6990–6997, 2021, pMID: 34387505. [Online]. Available: https://doi.org/10.1021/acs.nanolett.1c02331 5, 6

[34] Z. Wang and F. Pang, “A facile way to control phase of tin selenide flakes by chemical vapor deposition,” *Chemical Physics Letters*, vol. 702, pp. 90–95, 2018. [Online]. Available: https://www.sciencedirect.com/science/article/pii/S0009261418303610 6, 30

[35] B. An, Y. Ma, G. Zhang, C. You, and Y. Zhang, “Controlled synthesis of few-layer $SnSe_2$ by chemical vapor deposition,” *RSC Adv.*, vol. 10, pp. 42 157–42 163, 2020. [Online]. Available: http://dx.doi.org/10.1039/D0RA08360G 6, 30, 81

doi:10.6342/NTU202301860

[36] Y.-Y. Wang, “Two-Dimensional Mechano-Thermoelectric Heterojunctions for Self-Powered Sensors,” Master’s thesis, National Taiwan University, Taiwan, 2021. 6

[37] T.-H. Wang, “Epitaxially grown high quality tin diselenide on graphene at low temperature and its thickness dependent thermoelectric properties,” Master’s thesis, Chung Yuan Christian University, Taiwan, 2021. 7

[38] G. Konstantatos, “ Current status and technological prospect of photodetectors based on two-dimensional materials. ,” *Nat Commun*, vol. 9, p. 5266, 2018. 9

[39] M. Buscema, J. O. Island, D. J. Groenendijk, S. I. Blanter, G. A. Steele, H. S. J. van der Zant, and A. Castellanos-Gomez, “Photocurrent generation with two-dimensional van der waals semiconductors,” *Chem. Soc. Rev.*, vol. 44, pp. 3691–3718, 2015. [Online]. Available: http://dx.doi.org/10.1039/C5CS00106D 9, 12

[40] C. L. Novoselov K., Fal ko V., “A roadmap for graphene.” *Nature*, vol. 490, pp. 192–200, 2012. [Online]. Available: https://doi.org/10.1038/nature11458 9

[41] M. Mittendorff, S. Winnerl, J. Kamann, J. Eroms, D. Weiss, H. Schneider, and M. Helm, “Ultrafast graphene-based broadband THz detector,” *Applied Physics Letters*, vol. 103, no. 2, 07 2013, 021113. [Online]. Available: https://doi.org/10.1063/1.4813621 9

[42] N. S. Tian H., Chin M.L., “Optoelectronic devices based on two-dimensional transition metal dichalcogenides. ,” *Nano Res.*, vol. 9, p. 1543–1560, 2016. [Online]. Available: https://doi.org/10.1007/s12274-016-1034-9 10

[43] F. Wang, Z. Wang, L. Yin, R. Cheng, J. Wang, Y. Wen, T. A. Shifa, F. Wang, Y. Zhang, X. Zhan, and J. He, “2D library beyond graphene and transition metal dichalcogenides: a focus on photodetection,”

Chem. Soc. Rev., vol. 47, pp. 6296–6341, 2018. [Online]. Available: http://dx.doi.org/10.1039/C8CS00255J 12

[44] P. Yu, X. Yu, W. Lu, H. Lin, L. Sun, K. Du, F. Liu, W. Fu, Q. Zeng, Z. Shen, C. Jin, Q. J. Wang, and Z. Liu, "Fast Photoresponse from 1T Tin Diselenide Atomic Layers," *Advanced Functional Materials*, vol. 26, no. 1, pp. 137–145, 2016. [Online]. Available: https://onlinelibrary.wiley.com/doi/abs/10.1002/adfm.201503789 15

[45] M. Kumar, S. Rani, A. Pandey, K. S. Gour, S. Husale, P. Singh, and V. Singh, "Highly responsive, low-bias operated $SnSe_2$ nanostructured thin film for trap-assisted NIR photodetector," *Journal of Alloys and Compounds*, vol. 838, p. 155384, 2020. [Online]. Available: https://www.sciencedirect.com/science/article/pii/S0925838820317473 16

[46] M. Hempel, D. Nezich, J. Kong, and M. Hofmann, "A Novel Class of Strain Gauges Based on Layered Percolative Films of 2D Materials," *Nano Letters*, vol. 12, no. 11, pp. 5714–5718, 2012, pMID: 23045955. [Online]. Available: https://doi.org/10.1021/nl302959a 23

[47] K. S. Novoselov, A. K. Geim, S. V. Morozov, D. Jiang, Y. Zhang, S. V. Dubonos, I. V. Grigorieva, and A. A. Firsov, "Electric field effect in atomically thin carbon films," *Science*, vol. 306, no. 5696, pp. 666–669, 2004. [Online]. Available: https://www.science.org/doi/abs/10.1126/science.1102896 28

[48] Z. Cai, B. Liu, X. Zou, and H.-M. Cheng, "Chemical vapor deposition growth and applications of two-dimensional materials and their heterostructures," *Chemical Reviews*, vol. 118, no. 13, pp. 6091–6133, 2018, pMID: 29384374. [Online]. Available: https://doi.org/10.1021/acs.chemrev.7b00536 28

[49] Y. Huang, K. Xu, Z. Wang, T. A. Shifa, Q. Wang, F. Wang, C. Jiang, and J. He, "Designing the shape evolution of $snse_2$ nanosheets and their

optoelectronic properties," *Nanoscale*, vol. 7, pp. 17 375–17 380, 2015. [Online]. Available: http://dx.doi.org/10.1039/C5NR05989E 29

[50] Y.-P. Hsieh, M. Hofmann, and J. Kong, "Promoter-assisted chemical vapor deposition of graphene," *Carbon*, vol. 67, pp. 417–423, 2014. [Online]. Available: https://www.sciencedirect.com/science/article/pii/S0008622313009603 29

[51] L. Huang, Y. Yu, C. Li, and L. Cao, "Substrate Mediation in Vapor Deposition Growth of Layered Chalcogenide Nanoplates: A Case Study of $SnSe_2$," *The Journal of Physical Chemistry C*, vol. 117, no. 12, pp. 6469–6475, 2013. [Online]. Available: https://doi.org/10.1021/jp400274a 30

[52] D. Colombara, S. Delsante, G. Borzone, J. Mitchels, K. Molloy, L. Thomas, B. Mendis, C. Cummings, F. Marken, and L. Peter, "Crystal growth of Cu_2ZnSnS_4 solar cell absorber by chemical vapor transport with I_2," *Journal of Crystal Growth*, vol. 364, pp. 101–110, 2013. [Online]. Available: https://www.sciencedirect.com/science/article/pii/S0022024812008342 30

[53] R. Nitsche, H. Bölsterli, and M. Lichtensteiger, "Crystal growth by chemical transport reactions—I: Binary, ternary, and mixed-crystal chalcogenides," *Journal of Physics and Chemistry of Solids*, vol. 21, no. 3, pp. 199–205, 1961. [Online]. Available: https://www.sciencedirect.com/science/article/pii/0022369761900981 31

[54] J. D. Jackson, *Classical Electrodynamics*, 3rd ed. Wiley & Sons Ltd, 1998. 37

[55] Harris and Bertolucci, *Symmetry and Spectroscopy*. Dover Publications, 1989. 37

[56] D. A. Long, *The Raman Effect*. Wiley & Sons Ltd, 2002. 40

[57] G. Binnig, C. F. Quate, and C. Gerber, “Atomic force microscope,” *Phys. Rev. Lett.*, vol. 56, pp. 930–933, Mar 1986. [Online]. Available: https://link.aps.org/doi/10.1103/PhysRevLett.56.930 43

[58] M. Dunlap and D. J. E. Adaskaveg, *Introduction to the Scanning Electron Microscope*, 1997. 46

[59] J. I. Pankove, *Optical Processes in Semiconductors*. Courier Corporation, 1971. 48

[60] J. Tauc, R. Grigorovici, and A. Vancu, “Optical Properties and Electronic Structure of Amorphous Germanium,” *physica status solidi (b)*, vol. 15, no. 2, pp. 627–637, 1966. [Online]. Available: https://onlinelibrary.wiley.com/doi/abs/10.1002/pssb.19660150224 50

[61] E. A. Davis and N. F. Mott, “Conduction in non-crystalline systems V. Conductivity, optical absorption and photoconductivity in amorphous semiconductors,” *The Philosophical Magazine: A Journal of Theoretical Experimental and Applied Physics*, vol. 22, no. 179, pp. 0903–0922, 1970. [Online]. Available: https://doi.org/10.1080/14786437008221061 50

[62] P. Makuła, M. Pacia, and W. Macyk, “How to correctly determine the band gap energy of modified semiconductor photocatalysts based on UV–Vis spectra,” *The Journal of Physical Chemistry Letters*, vol. 9, no. 23, pp. 6814–6817, 2018. [Online]. Available: https://doi.org/10.1021/acs.jpclett.8b02892 50

[63] E. Ruiz-Trejo, “The optical band gap of Gd-doped CeO2 thin films as function of temperature and composition,” *Journal of Physics and Chemistry of Solids*, vol. 74, no. 4, pp. 605–610, 2013. [Online]. Available: https://www.sciencedirect.com/science/article/pii/S0022369712003800 50

[64] F. Urbach, “The long-wavelength edge of photographic sensitivity and of the electronic absorption of solids,” *Phys. Rev.*, vol. 92, pp. 1324–1324, Dec

1953. [Online]. Available: https://link.aps.org/doi/10.1103/PhysRev.92.1324 53

[65] J. Tauc and A. Menth, "States in the gap," *Journal of Non-Crystalline Solids*, vol. 8-10, pp. 569–585, 1972, amorphous and Liquid Semiconductors. [Online]. Available: https://www.sciencedirect.com/science/article/pii/0022309372901949 53

[66] N. Chopra, A. Mansingh, and G. Chadha, "Electrical, optical and structural properties of amorphous $V_2O_5TeO_2$ blown films," *Journal of Non-Crystalline Solids*, vol. 126, no. 3, pp. 194–201, 1990. [Online]. Available: https://www.sciencedirect.com/science/article/pii/0022309390908198 53

[67] D. Souri and K. Shomalian, "Band gap determination by absorption spectrum fitting method (ASF) and structural properties of different compositions of (60x) V_2O_5–$40TeO_2$–xSb_2O_3 glasses," *Journal of Non-Crystalline Solids*, vol. 355, no. 31, pp. 1597–1601, 2009. [Online]. Available: https://www.sciencedirect.com/science/article/pii/S0022309309003366 54

[68] A. L. R.J. Martín-Palma, "Vapor-deposition techniques," *Engineered Biomimicry*, pp. 383–398, 2013. 64

[69] E. Lorchat, G. Froehlicher, and S. Berciaud, "Splitting of Interlayer Shear Modes and Photon Energy Dependent Anisotropic Raman Response in N-Layer $ReSe_2$ and ReS_2," *ACS Nano*, vol. 10, no. 2, pp. 2752–2760, 2016, pMID: 26820232. [Online]. Available: https://doi.org/10.1021/acsnano.5b07844 74

[70] A. N. C.D. Wagner, "NIST Standard Reference Database 20," 2003. 77

[71] W. Dong, C. Lu, M. Luo, Y. Liu, T. Han, Y. Ge, X. Xue, Y. Zhou, and X. Xu, "Enhanced UV–Vis photodetector performance by optimizing interfacial charge transportation in the heterostructure by SnS and

$SnSe_2$," *Journal of Colloid and Interface Science*, vol. 621, pp. 374–384, 2022. [Online]. Available: https://www.sciencedirect.com/science/article/pii/S002197972200594X 77, 79

[72] S. Jin, D. Wu, W. Song, H. Hao, W. Gao, and S. Yan, "Superior acetone sensor based on hetero-interface of $SnSe_2/SnO_2$ quasi core shell nanoparticles for previewing diabetes," *Journal of Colloid and Interface Science*, vol. 621, pp. 119–130, 2022. [Online]. Available: https://www.sciencedirect.com/science/article/pii/S0021979722006130 79

[73] T. J. S. J. S. S. Seung Hwae Heo, Jae Sung Son, "Fabrication of high-performance $SnSe_2$ thermoelectric thin films with preferred crystallographic orientation." *Applied physics letters*, vol. 120, 2022. 84

[74] M. Muñoz Rojo, J. J. Romero, D. Ramos, D.-A. Borca-Tasciuc, T. Borca-Tasciuc, and M. Martín Gonzalez, "Modeling of transient thermoelectric transport in Harman method for films and nanowires," *International Journal of Thermal Sciences*, vol. 89, pp. 193–202, 2015. [Online]. Available: https://www.sciencedirect.com/science/article/pii/S1290072914002981 84

[75] C. Xie, C. Mak, X. Tao, and F. Yan, "Photodetectors Based on Two-Dimensional Layered Materials Beyond Graphene," *Advanced Functional Materials*, vol. 27, no. 19, p. 1603886, 2017. [Online]. Available: https://onlinelibrary.wiley.com/doi/abs/10.1002/adfm.201603886 96

doi:10.6342/NTU202301860